

Electron temperatures and densities of planetary nebulae determined from the nebular hydrogen recombination spectrum and temperature and density variations

Y. Zhang

Department of Astronomy, Peking University, Beijing 100871, China

National Astronomical Observatories, Chinese Academy of Sciences, Beijing 100012, China

zhangy@bac.pku.edu.cn

X.-W. Liu

Department of Astronomy, Peking University, Beijing 100871, China

R. Wesson

Department of Physics and Astronomy, University College London, Gower Street, London WC1E 6BT, UK

P. J. Storey

Department of Physics and Astronomy, University College London, Gower Street, London WC1E 6BT, UK

Y. Liu

Department of Astronomy, Peking University, Beijing 100871, China

Department of physics, Guangzhou University, Guangyuan Zhong Lu 248, Guangzhou 510405, China

and

I. J. Danziger

Osservatorio Astronomico di Trieste, Via G. B. Tiepolo 11, 1-34131 Trieste, Italy

ABSTRACT

A method is presented to derive electron temperatures and densities of planetary nebulae (PNe) simultaneously, using the observed hydrogen recombination

spectrum, which includes continuum and line emission. By matching theoretical spectra to observed spectra around the Balmer jump at about 3646 \AA , we determine electron temperatures and densities for 48 Galactic PNe. The electron temperatures based on this method [hereafter $T_e(\text{Bal})$] are found to be systematically lower than those derived from [O III] $\lambda 4959/\lambda 4363$ and [O III] $(88\mu\text{m} + 52\mu\text{m})/\lambda 4959$ ratios [hereafter, $T_e([\text{O III}]_{\text{na}})$ and $T_e([\text{O III}]_{\text{fn}})$]. And the electron densities based on this method are found to be systematically higher than those derived from [O II] $\lambda 3729/\lambda 3726$, [S II] $\lambda 6731/\lambda 6716$, [Cl III] $\lambda 5537/\lambda 5517$, [Ar IV] $\lambda 4740/\lambda 4711$ and [O III] $88\mu\text{m}/52\mu\text{m}$ ratios. These results suggest that temperature and density fluctuations are generally present within nebulae. The comparison of $T_e([\text{O III}]_{\text{na}})$ and $T_e(\text{Bal})$ suggests that the fractional mean-square temperature variation (t^2) has a representative value of 0.031. A majority of temperatures derived from the [O III] $(88\mu\text{m} + 52\mu\text{m})/\lambda 4959$ ratio are found to be higher than $T_e([\text{O III}]_{\text{na}})$, which is attributed to the existence of dense clumps in nebulae – those [O III] IR fine-structure lines are suppressed by collisional de-excitation in the clumps. By comparing $T_e([\text{O III}]_{\text{fn}})$, $T_e([\text{O III}]_{\text{na}})$ and $T_e(\text{Bal})$ and assuming a simple two-density-component model, we find that the filling factor of dense clumps has a representative value of 7×10^{-5} . The discrepancies between $T_e([\text{O III}]_{\text{na}})$ and $T_e(\text{Bal})$ are found to be anti-correlated with electron densities derived from various density indicators; high-density nebulae have the smallest temperature discrepancies. This suggests that temperature discrepancy is related to nebular evolution. In addition, He/H abundances of PNe are found to be positively correlated with the difference between $T_e([\text{O III}]_{\text{na}})$ and $T_e(\text{Bal})$, suggesting that He/H abundances might have been overestimated generally because of the possible existence of H-deficient knots. Electron temperatures and densities deduced from spectra around the Paschen jump regions at 8250 \AA are also obtained for four PNe, NGC 7027, NGC 6153, M 1-42 and NGC 7009. Electron densities derived from spectra around the Paschen jump regions are in good agreement with the corresponding values derived from spectra around the Balmer jump, whereas temperatures deduced from the spectra around the Paschen jump are found to be lower than the corresponding values derived from spectra around the Balmer jump for all the four cases. The reason remains unclear.

Subject headings: atomic processes – planetary nebulae: general – ISM: abundances

1. Introduction

Accurate determinations of metal abundances in planetary nebulae (PNe) are important for understanding the chemical evolution of galaxies and the nucleosynthesis and mixing processes in low- and intermediate-mass stars. A long-standing problem in nebular abundance studies has been that the heavy-element abundances derived from optical recombination lines (ORLs) are systematically higher than those derived from collisionally excited lines (CELs; see Liu 2001, 2003 for recent reviews). In extreme cases, the discrepancies exceed a factor of 10. Given that CEL abundances are sensitive to electron temperature and density, knowledge of temperature and density variations is an essential ingredient in understanding the abundance discrepancy problem. Information on temperature and density variations can be obtained by comparing results derived from plasma diagnostics which behave differently as temperature and density vary. Traditionally, nebular electron temperatures and densities are derived from CEL ratios. However, for PNe including high-density regions ($N_e \gtrsim 10^6 \text{ cm}^{-3}$), such as IC 4997 (Hyung et al. 1994), Mz 3 (Zhang & Liu 2002) and M 2-24 (Zhang & Liu 2003), CELs are strongly suppressed by collisional de-excitation, and so depending on their critical densities, they may become unusable in probing such high-density regions. On the other hand, hydrogen recombination lines have very high critical densities ($\gtrsim 10^8 \text{ cm}^{-3}$). Consequently, the hydrogen recombination spectrum provides a powerful tool to probe high-density regions. Comparison of electron temperatures and densities derived from the hydrogen recombination spectrum (lines plus continuum) with those derived from CELs should enable us to quantify temperature and density variations in nebulae.

By measuring the Balmer discontinuity, Liu & Danziger (1993) determined electron temperatures in 14 PNe and found that they are systematically lower than those derived from the [O III] nebular-to-auroral forbidden line ratio. This can be explained by the presence of large temperature fluctuations since the [O III] $\lambda 4363$ auroral line of higher excitation energy tends to be emitted in higher temperature regions than the [O III] $\lambda\lambda 4959, 5007$ nebular lines of lower excitation energy, as suggested by Peimbert (1967). Recent reviews on temperature fluctuations of gaseous nebulae are given by Torres-Peimbert (2003) and references therein. However, no photoionization models yield such large temperature fluctuations suggested by observations. Moreover, temperature fluctuations are unable to explain the large disparity between the ORL and CEL abundances observed in some PNe (Liu 2001). Instead, it is found that the hypothesis that PNe may contain clumps of different temperature, density and chemical composition, embedded in diffuse ‘normal’ material, can explain many of the observed patterns (Liu et al. 2000). Peimbert’s concept of temperature fluctuations alone may not be a realistic description of the physical conditions in a nebula, although it has proven to be a convenient and useful way to characterize the complexities of real nebulae.

It is expected that there are also variations of electron density inside a PN. Rubin (1989) pointed out that electron densities derived from various plasma diagnostics should correlate positively with the critical densities of the diagnostic lines involved if there are large density variations within a nebula. Liu et al. (2001a) found that electron densities derived from the [O III] $88\mu\text{m}/52\mu\text{m}$ ratios are generally lower than those derived from the optical [Ar IV] and [Cl III] doublet ratios, suggesting the presence of high density regions in PNe, where the 52- and $88\text{-}\mu\text{m}$ lines are suppressed by collisional de-excitation due to their relatively low critical densities. Viegas & Clegg (1994) showed that the discrepancies between $T_e([\text{O III}]_{\text{na}})$ and $T_e(\text{Bal})$ can be explained by the presence of condensations in nebulae and gave an analytical method of estimating the filling factor of condensations. Our detailed studies of the peculiar PNe Mz 3 and M 2-24 suggest that the presence of high-density regions in some PNe can significantly affect abundance determinations (Zhang & Liu 2002, 2003). However, density inhomogeneities alone cannot explain the large disparity between the ORL and CEL abundances either, unless the condensations are also H-deficient (Liu et al. 2000).

Liu et al. (2000) found that the discrepancy between the ORL and CEL abundances correlates with the difference between the temperatures derived from the [O III] collisional lines and from the Balmer jump of hydrogen recombination spectrum, thus lending strong support to the argument that some extremely cold H-deficient knots may co-exist with normal nebular material in many PNe. However, it is difficult to explain the origin and evolution of such H-deficient knots with the current theories of element production in intermediate-mass stars.

In this paper, we present determinations of electron temperatures and densities for a large sample of PNe based on the analysis of nebular hydrogen recombination spectrum. Section 2 describes the sample. In Section 3, we describe a new approach to deriving electron temperature and density simultaneously from the observed nebular hydrogen recombination spectrum (lines plus continuum) and present the results. In Section 4, we compare results derived from a variety of temperature and density indicators and discuss the significance of variations in electron temperature and density in PNe. A discussion of He/H abundance determinations is also presented in this Section. In Section 5, we present electron temperatures and densities derived from the Paschen discontinuity and decrements. A summary then follows in Section 6.

2. The sample

2.1. Observations and data reduction

48 Galactic PNe (37 disc PNe and 11 bulge PNe) are analyzed in the current work. The spectra were obtained in a series of observing runs using telescopes at ESO La Silla and La Palma.

14 objects were observed using the ISIS double long-slit spectrograph mounted on the 4.2 m William Herschel Telescope (WHT) at La Palma Observatory in 1996 July–August and in 1997 August. A Tek 1024 × 1024 24 μm × 24 μm charge coupled device (CCD) was used, which yielded a spatial sampling of 0.3576 arcsec per pixel projected on the sky. In 1996, a 600 g mm⁻¹ and a 316 g mm⁻¹ grating were used for the Blue and Red Arm, respectively. In 1997, they were replaced by a 1200 g mm⁻¹ grating.

23 objects were observed with the ESO 1.52 m telescope using the Boller & Chivens (B&C) long-slit spectrograph. The spectra were obtained during runs in 1995 July, 1996 July, 1997 February and 2001 June. In 1995 the detector was a Ford 2048 × 2048 15 μm × 15 μm chip, which was superseded in 1996 by a thinned UV-enhanced Loral 2048 × 2048 15 μm × 15 μm chip of much improved quantum efficiency. The B&C spectrograph has a useful slit length of about 3.5 arcmin. In order to reduce the CCD read-out noise, the CCD was binned by a factor of two along the slit direction, yielding a spatial sampling of 1.63 arcsec per pixel projected on the sky. A slit width of 2 arcsec was used throughout the ESO 1.52 m runs.

11 objects were observed using the Intermediate Dispersion Spectrograph (IDS) on the 2.5 m Isaac Newton Telescope (INT) at the Observatorio del Roque de los Muchachos, on La Palma, Spain in 2001 August. A slit 4 arcmin long and 1 arcsec wide was used for nebular observations. The R1200B grating was used to cover wavelengths from 3500–5000 Å at a spectral resolution of 0.95 Å, determined from the *FWHM* of the calibration arc lines, while the R300V grating, together with a GG385 order sorting filter, was used to cover wavelengths from 3800–7700 Å at a resolution of 4.0 Å *FWHM*.

All the spectra were reduced using MIDAS¹ or IRAF² following the standard procedure. The spectra were bias-subtracted, flat-fielded and cosmic-rays removed, and then wavelength calibrated using exposures of a calibration arc lamp. The spectra were flux-calibrated by observing spectrophotometric standard stars. 1-D spectra were obtained by integrating along the slit. Using the Galactic reddening law of Howarth (1983), the log-

¹MIDAS is developed and distributed by the European Southern Observatory.

²IRAF is developed and distributed by the National Optical astronomy Observatory.

arithmetic extinction at $H\beta$, $c = \log I(H\beta)/F(H\beta)$, was derived from the observed Balmer decrements, the $H\alpha/H\beta$, $H\gamma/H\beta$ and $H\delta/H\beta$ ratios. A mean value for each nebula was used to deredden the spectra. The object names and the extinction constants are given in Table 1.

Amongst the PNe in our sample, far-infrared spectra for 21 of them have been obtained using the Long Wavelength Spectrometer (LWS) on board the Infrared Space Observatory (*ISO*). Fluxes of far-IR fine structure lines derived from these spectrum have been published by Liu et al. (2001a) except for three objects, Hu 1-2, NGC 6210 and NGC 6818. For the latter three PNe, we measured far-IR line fluxes using spectra retrieved from the *ISO* data archive. In order to normalize the *ISO* line fluxes to $H\beta$, the absolute $H\beta$ fluxes tabulated in Cahn et al. (1992) were used.

2.2. He^+/H^+ and $\text{He}^{2+}/\text{H}^+$ abundance ratios

In order to calculate theoretical nebular spectra, accurate determinations of the He^+/H^+ and $\text{He}^{2+}/\text{H}^+$ abundance ratios are necessary (see Section 3). Helium ionic abundances were derived from He I and He II recombination lines, using

$$\frac{N(\text{He}^{i+})}{N(\text{H}^+)} = \frac{I_\lambda}{I_{H\beta}} \frac{\lambda}{\lambda_{H\beta}} \frac{\alpha_{H\beta}}{\alpha_{\text{He}^{i+}}}, \quad (1)$$

which have only a weak dependence on the adopted electron temperature and density.

He^+/H^+ abundance ratios were calculated from the strong line He I $\lambda 5876$ under the assumption of Case A. The effective recombination coefficient $\alpha_{\text{He}^+_{5876}}$ is derived from the formulae presented by Benjamin et al. (1999). $\text{He}^{2+}/\text{H}^+$ abundance ratios were calculated from the He II $\lambda 4686$ line, using the effective recombination coefficient $\alpha_{\text{He}^{2+}_{4686}}$ of Storey & Hummer (1995). The results are presented in Table 1.

2.3. Temperature and Density determined from far-IR and optical forbidden line ratios

For the purpose of comparison, various forbidden line ratios are also used to determine electron temperatures and densities. For densities, results derived from the following diagnostic ratios were used, $[\text{O III}] 52 \mu\text{m}/88 \mu\text{m}$, $[\text{O II}] \lambda 3729/\lambda 3726$, $[\text{S II}] \lambda 6716/\lambda 6731$, $[\text{Cl III}] \lambda 5517/\lambda 5537$ and $[\text{Ar IV}] \lambda 4711/\lambda 4740$. Electron densities from the $[\text{O III}] 52\text{-}\mu\text{m}/88\text{-}\mu\text{m}$ ratio are taken from Liu et al. (2001a) except for NGC 6210 and NGC 6818, for which we obtain the values of $\log N_e = 3.19$ and 2.86 (cm^{-3}), respectively, using our own measured

line fluxes. Densities deduced from the optical [O II] $\lambda 3729/\lambda 3726$, [S II] $\lambda 6716/\lambda 6731$, [Cl III] $\lambda 5517/\lambda 5537$ and [Ar IV] $\lambda 4711/\lambda 4740$ doublet ratios are taken from Wang et al. (in preparation). A detailed discussion of these density indicators is given in their paper.

Electron temperatures derived from the [O III] $(88\mu\text{m} + 52\mu\text{m})/\lambda 4959$ and [O III] $\lambda 4959/\lambda 4363$ ratios together with their uncertainties are presented in Table 1. For the former, values were derived assuming electron densities derived from the [O III] $52\text{-}\mu\text{m}/88\text{-}\mu\text{m}$ line ratio. For the latter, the average densities derived from the [Cl III] $\lambda 5517/\lambda 5537$ and [Ar IV] $\lambda 4711/\lambda 4740$ doublet line ratios were adopted, given that Cl^+ and Ar^{2+} have ionization potentials of 23.8 eV and 40.7 eV, respectively, comparable to the value of 35.1 eV for O^+ , and therefore anticipating that the [O III] lines arise from similar ionized regions as [Cl III] and [Ar IV] lines. As the density increases, the resultant temperatures become increasingly sensitive to the adopted density. When the density reaches a value higher than 10^6 cm^{-3} , the [O III] $(88\mu\text{m} + 52\mu\text{m})/\lambda 4959$ and [O III] $\lambda 4959/\lambda 4363$ ratios are no longer useful temperature diagnostics. For example, high density regions have been detected in M 2-24 and IC 4997 (Zhang & Liu 2003; Hyung et al. 1994). For both PNe, temperatures deduced from the [O III] $\lambda 4959/\lambda 4363$ ratio have large uncertainties.

3. Electron temperature and density determined from the hydrogen recombination spectrum

The H I recombination spectrum consists of continuum and line emission. The continuous spectrum has a jump at the limit of the Balmer series at 3646 Å. High-order Balmer lines ($n \rightarrow 2$, $n \gtrsim 25$) converge at the Balmer discontinuity and merge with the continuum jump at shorter wavelength. The size of the Balmer jump is a function of electron temperature. On the other hand, intensities of high-order Balmer lines ($n \rightarrow 2$, $n \gtrsim 10$) relative to $\text{H}\beta$ are sensitive to electron density. Therefore, the hydrogen recombination spectrum near the Balmer jump region provides valuable temperature and density diagnostics. Our method and results of the electron temperature and density determinations based on this technique are presented below.

3.1. Theoretical spectra

Several processes contribute to the continuum emission from a nebula: free-free and free-bound emission and the two-photon decay. Apart from hydrogen, the second most abundant element, helium also contributes significantly to the first two processes. In addition, emission

from the central star and local dust can in principle contaminate the observed continuum spectrum. In the following, a detailed calculation including all the processes is presented.

The free-free (or bremsstrahlung) emission, which is emitted when an free electron interacts but does not combine with a positively charged ion such as H^+ , He^+ and He^{2+} , dominates the nebular continuum in the infrared and radio region. The emission coefficient of this process is given by Brown & Mathews (1970),

$$j_{\nu,ff} = \frac{1}{4\pi} N_i N_e \frac{32Z^2 e^4 h}{3m_e^2 c^3} \left(\frac{\pi h \nu_0}{3kT_e}\right)^{1/2} e^{-h\nu/kT_e} g_{ff} \text{ [erg cm}^{-3} \text{ s}^{-1} \text{ Hz}^{-1}\text{]}, \quad (2)$$

where N_i and N_e are ion and electron densities respectively, Z is the nuclear charge, T_e is the electron temperature, $h\nu_0$ denotes the Rydberg energy and g_{ff} is the free-free Gaunt factor. Here g_{ff} is computed using the method outlined by Hummer (1988).

In the optical region, free-bound emission is the main contributor to the continuum. According to Brown & Mathews (1970), the emission coefficient of continuous emission due to recombinations of H^+ , He^+ or He^{2+} with electrons is

$$j_{\nu,bf} = \frac{1}{4\pi} N_i N_e \frac{\pi h^4 \nu^3}{c^2} \left(\frac{2}{\pi m_e k T_e}\right)^{3/2} \sum_{n=n_1}^{\infty} \sum_{l=0}^{n-1} n^2 a_{nl}(\nu) e^{h(\nu_{nl}-\nu)/kT_e} \text{ [erg cm}^{-3} \text{ s}^{-1} \text{ Hz}^{-1}\text{]}, \quad (3)$$

where $h\nu_{nl}$ is the ionization potential of the (n,l) state, n_1 is the lowest state that can contribute to the free-bound emission at the given frequency ν and $a_{nl}(\nu)$ is the photoionization cross-section for the state, which is computed using the method described by Storey & Hummer (1991).

Another important source of continuous emission is two-photon decay of the 2^2S level of the hydrogen atom (two-photon emission from He^+ and He^0 is negligible for nebulae of cosmic compositions; Brown & Mathews, 1970). Single photon transition from the 2^2S level to the ground 1^2S is forbidden. Radiative decay of the 2^2S level to the ground can only occur via two photon emission, in which the electron jumps to a virtual level, which can lie in anywhere between $n = 1$ and $n = 2$ levels, and then to the ground state, emitting two photons in the process. As a result, continuum emission longward of $Ly\alpha$ will occur. The emission coefficient of the two-photon process is given by

$$j_{\nu,2q} = \frac{1}{4\pi} n_{2^2S} h \nu A(y) \text{ [erg cm}^{-3} \text{ s}^{-1} \text{ Hz}^{-1}\text{]}, \quad (4)$$

where $y = \nu/\nu_{Ly\alpha}$ and $A(y)dy$ is the probability per second for emitting a photon in the interval dy . Approximately, the function $A(y)$ is given by the following expression

$$A(y) = 202.0\{y(1-y)\{1 - [4y(1-y)]^{0.8}\} + 0.88[y(1-y)]^{1.53}[4y(1-y)]^{0.8}\}s^{-1} \quad (5)$$

(Kwok 2000). The transition probability for the two-photon decay is $A_{2^2S,1^2S} = \int_0^1 A(y)dy = 8.23 \text{ s}^{-1}$. The equilibrium population of the 2^2S state is given by

$$n_{2^2S} = \frac{N_p N_e \alpha_{2^2S}^{eff}}{A_{2^2S,1^2S} + N_p q_{2^2S,2^2P}^p + N_e q_{2^2S,2^2P}^e} \quad (6)$$

(Osterbrock 1989), where N_p is the proton density, $\alpha_{2^2S}^{eff}$ is the effective recombination coefficient for populating 2^2S , and $q_{2^2S,2^2P}^p$ and $q_{2^2S,2^2P}^e$ are the collisional de-excitation transition rates of 2^2S to 2^2P states by electrons and protons, respectively. Note that the collisional transition from 2^2P to 2^2S has been ignored in equation (6). Under Case A conditions, this is a good approximation. Under Case B conditions, however, the population of the 2^2P state is comparable to that of the metastable 2^2S level since Ly α is trapped between the 2^2P and 1^2S states. Consequently, there is considerable collisional excitation from 2^2P to 2^2S , which enhances the two-photon emission. Therefore, the emission coefficient of two-photon process given by equation (4) can be significantly underestimated. However, this hardly affects our resultant electron temperatures and densities since an additional continuum (see below), is added to fit our observed spectrum in order to simulate direct and scattered stellar light. For a limited wavelength region, such an approach is sufficient to account for any excess emission from the two-photon process.

Finally, direct or scattered light from the central star can contaminate the observed continuum level. For our observations, the slit position was normally chosen to sample the brightest parts of the nebulae, sometimes passing through the central star. Some spectra were derived by scanning across the nebular surface. It is quite difficult to evaluate the level and spectral energy distribution of the contaminating stellar continuum. As central stars of PNe are relatively hot ($\gtrsim 20,000 \text{ K}$), in our calculation, a Rayleigh-Jeans approximation for a Black Body ($j_{\lambda,RJ} \propto \lambda^{-4}$) is adopted to simulate the stellar continuum. This stellar component also partially compensates for the underestimated two-photon continuum, as mentioned above. For simplicity, we shall call this term ‘stellar continuum’ hereafter. Continuum emission from dust grains peaks in the infrared and is negligible in the optical region. Thus it has been neglected in our calculation.

Apart from continuum emission, recombination line emission from bound-bound transitions of H^0 , He^0 and He^+ is also included. The emission coefficient of a recombination line is given by

$$j_{k,bb} = \frac{1}{4\pi} N_e N_i \alpha_k^{eff} h\nu_k [\text{erg cm}^{-3} \text{ s}^{-1}], \quad (7)$$

where α_k^{eff} is the effective recombination coefficient of the line. For H I and He II recombination lines, emission coefficients are determined as in Hummer & Storey (1987). Here the considered maximum principle quantum number of is $n = 500$. For He I recombination lines,

emission coefficients are taken from Benjamin et al. (1999) and Brocklehurst (1972). All line profiles are assumed Gaussian with a *FWHM*

$$\sigma_k = \sqrt{\sigma_{k,t}^2 + \sigma_o^2} \text{ \AA}, \quad (8)$$

where $\sigma_{k,t}$ is the *FWHM* caused by thermal broadening, given by

$$\sigma_{k,t} = 2\sqrt{\ln 2}\lambda_k \left(\frac{kT_e}{mc^2}\right)^{1/2} \text{ \AA}, \quad (9)$$

where m is the mass of the atom, and σ_o is the *FWHM* caused by other broadening effects, such as nebular expansion, turbulence, seeing conditions and instrument. For a typical PN observed here, $\sigma_o \gtrsim 8\sigma_{k,t}$. Line emission coefficients are thus converted into emission coefficients per unit wavelength by

$$j_{\lambda,bb} = \sum_k \frac{1}{\sigma_k \sqrt{2\pi}} \exp\left(-\frac{(\lambda - \lambda_k)^2}{2\sigma_k^2}\right) j_{k,bb} [\text{erg cm}^{-3} \text{ s}^{-1} \text{ \AA}^{-1}]. \quad (10)$$

Just longward of the Balmer jump, high-order Balmer lines converge and merge into a continuum-like feature. The slope of the feature is sensitive to electron density, and thus provide an excellent density diagnostic. The region is contaminated by the Ne II $\lambda 3664$ line of Multiplet V 1. However, the weak Ne II recombination line has a relatively narrow line width compared to the profile of the continuum-like feature and consequently, cannot cause any difficulty in our analysis.

Summing up contributions from all the processes discussed above, the flux at a given wavelength is given by

$$j_{\lambda,tot} = j_{\lambda,2q} + j_{\lambda,RJ} + \sum_{X=\text{H}^0, \text{He}^0, \text{He}^+} [j_{\lambda,ff}(X) + j_{\lambda,bf}(X) + j_{\lambda,bb}(X)] [\text{erg cm}^{-3} \text{ s}^{-1} \text{ \AA}^{-1}]. \quad (11)$$

Equation (11) shows that, in order to synthesize the nebular spectrum near the Balmer jump wavelength region, the required input parameters include nebular electron temperature and density, the magnitude of contaminating stellar continuum, He^+/H^+ and $\text{He}^{2+}/\text{H}^+$ ionic abundance ratios and σ_o . In general, decreasing (increasing) of the nebular electron temperature will steepen (flatten) the general shape of the theoretical continuum and increase (decrease) the Balmer discontinuities; decreasing (increasing) of electron density will steepen (flatten) the continuous feature redwards of 3646 \AA and decrease (increase) the intensities of high-order Balmer lines relative to a low-order line, such as $\text{H}\beta$, as shown in Fig. 1. Accordingly, matching the dereddened observed spectrum to those calculated from equation (11) by varying the electron temperature and density, we can determine the electron temperature and density simultaneously provided other parameters, such as He^+/H^+ and $\text{He}^{2+}/\text{H}^+$ abundance ratios and σ_o are known.

3.2. Results

Electron temperatures and densities for 48 PNe are derived by fitting the synthetic to the observed spectra. For synthesis, the required He^+/H^+ and $\text{He}^{2+}/\text{H}^+$ abundance ratios have been observationally determined, and σ_o was derived by fitting the line profiles of strong H I recombination lines deconvolved with the thermal broadening, as listed in Table 1. Three free parameters, nebular electron temperature and density and the fraction of the scattered Rayleigh-Jeans stellar continuum, are optimized simultaneously, using least Chi square method to match the observed spectra. For the optimization, the fitted data points were specified explicitly by eye, within the wavelength range from 3550–3850 Å, but excluding regions of strong (forbidden) lines. The results are partially shown in Fig. 2 together with the residuals of the fits.

In Table 2, we report the derived electron temperatures and densities along with their estimated errors. The Balmer jump and decrement of the H I recombination spectrum have previously been used to determine nebular electron temperatures and densities in four PNe, M 2-24 (Zhang & Liu 2003), NGC 6153 (Liu et al. 2000), M 1-42 and M 2-36 (Liu et al. 2001b). For the four PNe, the results derived here are in good agreement with the earlier results within the errors.

3.3. Error analysis

The errors caused by uncertainties in the input parameters He^+/H^+ and $\text{He}^{2+}/\text{H}^+$ abundance ratios are negligible due to the small measurement errors of strong He I and He II lines and their small contribution to the continuum emission compared to hydrogen ($\sim 10\%$). Errors in σ_o can also be ignored as this quantity is well determined by fitting strong hydrogen lines.

The complicated velocity fields within a nebula can cause different lines to have different deviations from their laboratory wavelengths, and thus can affect the quality of line-fitting made under the simple assumption of a uniform velocity for all ions and lines. Line-fitting can also be affected by blends of unknown lines and deviations of line profiles from Gaussian. Inspection of Fig. 2 shows that the observed intensities of the He I $2s^1S-5p^1P^o$ $\lambda 3614$ lines are generally lower than its predicted values. Liu et al. (2001b) attributed this to the destruction of He I Lyman photons by photoionization of H^0 or by absorption of dust grains. The wavelength region near the Balmer jump also contains a few strong O III Bowen fluorescence lines which are not considered in our simulations, thus giving large residuals at the corresponding wavelengths. However, these effects do not contribute to errors in the

derived electron temperatures and densities since these wavelengths have been excluded in the fitting.

The observed spectra plotted in Fig. 2, were de-reddened using extinction constants listed in Table 1. All spectra were normalized to H 11 λ 3770 in order to minimize errors in derived temperatures and densities caused by uncertainties in the reddening correction and flux calibration, and taking the advantage of the small wavelength difference between the Balmer jump and H 11.

The stellar continuum may have a spectral energy distribution that deviates from the Rayleigh-Jeans approximation adopted here. However, this continuum is expected to be smooth and vary only slightly over such a short wavelength range of fitting. Therefore, we have also ignored any possible errors caused by the fitting of the stellar continuum.

Errors in the derived temperatures and densities are dominated by two effects. Noise is an important source of error. For most PNe, we found that uncertainties due to this factor are about 5% in the derived temperatures and 0.1 dex in the densities. The other major error source originates from the extensive wings of the strong [O II] $\lambda\lambda$ 3726, 3729 lines, which can affect the shape of the continuum near the Balmer jump. The effect is larger for low-excitation PNe, such as NGC 40 and NGC 6720. The extensive wings of the [O II] lines can cause the continuum redwards of the Balmer jump to be overestimated. As a result, the temperatures can be overestimated. The errors can be reduced by including data points at longer wavelengths in the fitting, where the extensive wings of the [O II] lines have less impact. However, increasing the wavelength range of the fitting would increase uncertainties in the reddening correction and in fitting the stellar continuum. To evaluate errors due to this effect, each spectrum was fitted twice for two wavelength ranges with one extending further into the red than the other. The extensive wings of the [O II] lines can also decrease the shape of the continuum-like feature redwards of the Balmer jump, leading to overestimated densities. For most PNe, this effect is negligible given the large wavelength difference (about 70 Å) between the Balmer jump and the moderate strength of [O II] lines. However, the effect can be significant for those with extremely strong [O II] lines. On the other hand, the extensive wings of the [O II] lines have much less effect on the integrated intensities of high-order Balmer lines ($n \rightarrow 2$, $n = 11, 13, \dots, 23$) which can be determined using a line profile fitting technique. Comparison of densities derived from the continuum-like feature redwards of the Balmer jump with those deduced from the integrated intensities of high-order Balmer lines (e.g. Liu et al. 2001b) allows us to estimate the errors in the derived densities caused by the extensive wings of the [O II] lines. The final errors given in Table 2 were based on estimates of contributions from the two dominating sources of uncertainty discussed above.

4. Discussion

4.1. Comparison of densities

Electron densities deduced from the Balmer decrements, and from the [O II] $\lambda 3729/\lambda 3726$, [S II] $\lambda 6716/\lambda 6731$, [Cl III] $\lambda 5517/\lambda 5537$ and [Ar IV] $\lambda 4711/\lambda 4740$ doublet ratios are compared in Fig. 3. Fig. 3 shows that for most PNe, the hydrogen recombination spectrum yields higher densities compared to forbidden lines diagnostics. There is a trend such that the discrepancy becomes larger at higher densities. Two extreme cases are IC 4997 and M 2-24. For IC 3568, [Cl III] $\lambda 5517/\lambda 5537$ yields an abnormally low density. The cause of it is unclear but is probably due to measurement error. In Fig. 4 we compare electron densities derived from the [O III] far-infrared fine structure line ratio and from the hydrogen recombination spectrum. Evidently, densities derived from the [O III] $52\mu\text{m}/88\mu\text{m}$ ratio are significantly lower than those derived from the Balmer decrements. In fact, it has been found that the far-IR lines yield systematic lower densities, lower than even those deduced from optical forbidden line density-diagnostics (Liu et al. 2001a). A linear fit shows that the density discrepancy increases with the electron density.

O^0 , S^0 , Cl^+ , O^+ and Ar^{2+} have ionization potentials of 13.6, 10.4, 23.8, 35.1 and 40.7 eV, respectively, and therefore embrace a wide range of regions of differing states of ionization. On the other hand, the hydrogen recombination spectrum arises from the entire ionized nebula. Thus the discrepancies between densities derived from H I recombination spectrum and those deduced from forbidden line ratios are not likely to be caused by ionization stratifications. We notice that the [O II], [S II], [Cl III], [Ar IV] and [O III] density-diagnostic lines have critical densities of $N_{\text{crit}} \lesssim 10^5 \text{ cm}^{-3}$. Therefore, if the nebulae contain regions of higher densities, these forbidden lines will be suppressed in these regions by collisional de-excitation. In contrast, the hydrogen recombination spectrum is practically unaffected by collisional de-excitation. As a result, in such cases the hydrogen recombination spectrum will yield higher average densities compared to the [O II], [S II], [Cl III], [Ar IV] and [O III] lines ratios. The same argument has been developed by (Liu et al. 2001a) to explain the systematically lower densities derived from the [O III] fine-structure line ratio compare to those deduced from optical forbidden line ratios. The [Ar IV] lines have higher critical densities than the [O II], [S II], [Cl III] lines. Thus, the effects are weaker for [Ar IV] doublet ratio than for the other cases. Given that the [O III] far-infrared fine-structure lines have the lowest critical densities amongst those density-diagnostic forbidden lines ($N_{\text{cri}}([\text{O III}]_{\text{ff}}) \lesssim 4 \times 10^3 \text{ cm}^{-3}$), the effects are largest for the [O III] $52\mu\text{m}/88\mu\text{m}$ ratio. This can be seen clearly in Fig. 3 and Fig. 4. A nebular model including these high-density condensations and their effects on temperature determinations will be discussed in Section 4.3.

4.2. Comparison of temperatures

Fig. 5 and Fig. 6 show that electron temperatures derived from the [O III] $\lambda 4959/\lambda 4363$ and $(52\mu\text{m} + 88\mu\text{m})/\lambda 4959$ ratios [hereafter, $T_e([\text{O III}]_{\text{na}})$ and $T_e([\text{O III}]_{\text{fn}})$] are systematically higher than those deduced from the hydrogen recombination spectrum [hereafter $T_e(\text{Bal})$], although there are a few exceptions where $T_e(\text{Bal})$ is higher than $T_e([\text{O III}]_{\text{na}})$. The most extreme case is He 2-118, for which $T_e(\text{Bal})$ is 5000 K higher than $T_e([\text{O III}]_{\text{na}})$. In our sample, the four PNe with the largest temperatures discrepancies, Hf 2-2, M 1-42, M 2-36 and NGC 6153, were previously studied in detail by Liu (2003), Liu et al. (2001b) and Liu et al. (2000).

The discrepancy between $T_e([\text{O III}]_{\text{na}})$ and $T_e(\text{Bal})$ was first discovered by Peimbert (1971) and was attributed to temperature fluctuations within the nebula (Peimbert 1967). He characterized the temperature structure of a nebula by the average temperature T_0 and a mean square temperature fluctuation t^2 as follows:

$$T_0(N_e, N_i) = \frac{\int T_e N_e N_i dV}{\int N_e N_i dV} \quad (12)$$

and

$$t^2 = \frac{\int (T_e - T_0)^2 N_e N_i dV}{T_0^2 \int N_e N_i dV}, \quad (13)$$

where N_i is the ion density for an observed emission line. Assuming that all the oxygen is twice ionized and that there are no density and composition variations in the nebula, T_0 and t^2 can be derived from two of the three expressions,

$$T_e([\text{O III}]_{\text{na}}) = T_0 \left[1 + \frac{1}{2} \left(\frac{9.13 \times 10^4}{T_0} - 3 \right) t^2 \right], \quad (14)$$

$$T_e([\text{O III}]_{\text{fn}}) = T_0 \left[1 + \frac{1}{2} \left(\frac{2.92 \times 10^4}{T_0} - 3 \right) t^2 \right], \quad (15)$$

and

$$T_e(\text{Bal}) = T_0 (1 - 1.67 t^2), \quad (16)$$

(Peimbert 1967; Dinerstein et al. 1985).

In Fig. 5 and Fig. 6, lines showing $T_e([\text{O III}]_{\text{na}})$ as a function of $T_e(\text{Bal})$ for the case of $t^2 = 0.00, 0.02, 0.06$ and 1.00 are over plotted. Fig. 5 shows that most nebulae have $t^2 \lesssim 0.06$. Excluding a few extreme nebulae having $t^2 > 0.1$, we obtain a mean value of $\langle t^2 \rangle = 0.031$. The value is in excellent agreement with previous result $\langle t^2 \rangle = 0.03$ derived by Liu & Danziger (1993) although their analysis contained larger measurement errors. However, even excluding the extreme nebulae, a similar comparison between $T_e([\text{O III}]_{\text{fn}})$ and $T_e(\text{Bal})$

yields an average $\langle t^2 \rangle = 0.162$. As we shall show in the following subsection, it is likely that $T_e([\text{O III}]_{\text{fn}})$ have been overestimated because of density variations in the nebula, resulting in higher $\langle t^2 \rangle$ when comparing $T_e([\text{O III}]_{\text{fn}})$ and $T_e(\text{Bal})$.

Another interesting point revealed by Fig. 5 is that $T_e(\text{Bal})$ covers a wider range of values than $T_e([\text{O III}]_{\text{na}})$. Except a few extreme cases, $T_e([\text{O III}]_{\text{na}})$ falls between 8000 and 14000 K, whereas $T_e(\text{Bal})$ varies from 900 to 19000 K. Peimbert (1967) has argued that temperature fluctuations of gaseous nebulae can cause lower $T_e(\text{Bal})$ compared to $T_e([\text{O III}]_{\text{na}})$. However, even $\langle t^2 \rangle = 0.031$ is beyond any photoionization model prediction. Another explanation of higher $T_e(\text{Bal})$ compared to $T_e([\text{O III}]_{\text{na}})$ is that there are some condensations with $N_e > 10^6 \text{ cm}^{-3}$ in PNe, which then suppress the $T_e([\text{O III}])$ $\lambda\lambda 4959, 5007$ relative to the $\lambda 4363$, leading to an artificially higher $T_e([\text{O III}]_{\text{na}})$ (Viegas & Clegg 1994). But no such high density condensations have been found in PNe having extremely large temperature discrepancies (Liu et al. 2000, 2001b). Recently, Liu et al. (2000) presented an empirical nebular model containing two components, each with its own temperature, density and chemical composition to account for the temperature discrepancy. This seems to be the most plausible explanation at present.

For PNe having $T_e(\text{Bal}) > T_e([\text{O III}]_{\text{na}})$, as in He 2-118, the electron temperature might conceivably increase in low-ionization regions owing to heating by shock waves in the outer regions. As a result, the average temperature of the entire nebula [$T_e(\text{Bal})$] appears higher than that of high-ionization regions [$T_e([\text{O III}]_{\text{na}})$].

4.3. A simple model with condensations

In § 4.1, we found that electron densities derived from the H I recombination spectrum are systematically higher than those derived from optical forbidden lines ratios, and confirm the earlier result of Liu et al. (2001a) that densities derived from the [O III] far-IR fine-structure lines are the lowest of all. These results show that nebular electron densities derived from various diagnostics are correlated with the critical density of the diagnostic lines, and suggest that dense clumps are generally present in PNe.

In such cases, the [O III] $(52\mu\text{m} + 88\mu\text{m})/\lambda 4959$ ratio is no longer a good temperature indicator given the relatively low critical densities of the [O III] $52\mu\text{m}$ - and $88\mu\text{m}$ lines (3500 and 1500 cm^{-3} , respectively). When nebulae contain condensations with densities in the range between 10^4 and 10^6 cm^{-3} , the [O III] $52\mu\text{m}$ - and $88\mu\text{m}$ far-infrared lines will be heavily suppressed by collisional de-excitation, leading to overestimates of $T_e([\text{O III}]_{\text{fn}})$. On the other hand, condensations of densities in this range will not affect $T_e([\text{O III}]_{\text{na}})$ given

that the [O III] $\lambda 4959$ and $\lambda 4363$ lines have higher critical densities of $7 \times 10^5 \text{ cm}^{-3}$ and $3 \times 10^7 \text{ cm}^{-3}$, respectively (cf. Fig. 6).

Another piece of evidence pointing to the presence of dense clumps comes from Fig. 7 where we compare $T_e([\text{O III}]_{\text{na}})$ and $T_e([\text{O III}]_{\text{fn}})$. If nebulae have temperature fluctuations but are homogeneous in density, then $T_e([\text{O III}]_{\text{fn}})$ is expected to be always lower than $T_e([\text{O III}]_{\text{na}})$ (Dinerstein et al. 1985). However, Fig. 7 shows about two-third of the objects have higher $T_e([\text{O III}]_{\text{fn}})$ compared to $T_e([\text{O III}]_{\text{na}})$, suggesting that density variations play an important role in $T_e([\text{O III}]_{\text{fn}})$ determinations.

Viegas & Clegg (1994) showed that electron temperatures derived from the [O III] $\lambda 4363/(\lambda \lambda 4959 + 5007)$ ratio may be overestimated if nebulae contain ionized condensations of electron densities higher than 10^6 cm^{-3} . However, except for a few extreme PNe, such as IC 4997 (Hyung et al. 1994), Mz 3 (Zhang & Liu 2002) and M 2-24 (Zhang & Liu 2003) there is no evidence that nebulae contain a substantial amount of ionized gas in condensations with densities in excess of 10^6 cm^{-3} , as the presence of such condensations should have been revealed by the H I recombination spectrum (Liu et al. 2000, 2001a, 2001b; Fig. 3). Therefore, we consider $N_e \sim 10^5 \text{ cm}^{-3}$ as a safe upper limit for the density of these condensations.

In order to estimate the filling factor of the condensations, we use an analytical method originally developed by Viegas & Clegg (1994) for explaining the discrepancy of $T_e([\text{O III}]_{\text{na}})$ and $T_e(\text{Bal})$. Assuming that some high-density regions ($N_e > 10^6 \text{ cm}^{-3}$) are present, they deduced nebular-to-auroral [O III] line ratios (see their Eq. 2.3). Following the same deduction of their Eq. 2.3 but assuming that the electron density of these condensations is about 10^5 cm^{-3} instead of 10^6 cm^{-3} , we obtain the infrared-to-auroral line ratio

$$\frac{I_{52\mu\text{m}+88\mu\text{m}}}{I_{4959}} = \frac{\varepsilon_{\text{fL}}}{\varepsilon_{\text{nL}}} \frac{1 + \mu^2 \omega (\varepsilon_{\text{fH}}/\varepsilon_{\text{fL}})}{1 + \mu^2 \omega (\varepsilon_{\text{nH}}/\varepsilon_{\text{nL}})}, \quad (17)$$

where ε is line emission coefficient, $4\pi j = n_e n_i \varepsilon$, f and n refer to IR fine-structure line and nebular line, L and H refer to the low- and high-density regions, $\mu = (N_e)_{\text{H}}/(N_e)_{\text{L}}$ is the density contrast and $\omega = V_{\text{H}}/V_{\text{L}}$ is the filling factor. In the following calculation, we assume that: 1) density variations are the only cause of the lower $T_e([\text{O III}]_{\text{fn}})$ compared to $T_e([\text{O III}]_{\text{na}})$ and $T_e(\text{Bal})$; 2) the nebular gas has a homogeneous electron temperature, i.e., $T_e([\text{O III}]_{\text{na}})$ or $T_e(\text{Bal})$; 3) the condensations have densities lower than the critical density of the [O III] auroral line but higher than the critical densities of the [O III] infrared lines, whereas low-density regions have a density that is lower than the critical densities of the [O III] auroral and infrared lines.

Setting $F(T_{[\text{O III}]_{\text{fn}}}) = I_{52\mu\text{m}+88\mu\text{m}}/I_{4959}$, we have $\varepsilon_{\text{fL}}/\varepsilon_{\text{nL}} = F(T_{\text{Bal}})$. For a simple assumption $(N_e)_{\text{H}} = 10^5 \text{ cm}^{-3}$ and $(N_e)_{\text{L}} = 10^3 \text{ cm}^{-3}$, the ratio $\varepsilon_{\text{fH}}/\varepsilon_{\text{fL}}$ is about 0.04,

whereas ε_n is practically independent of the density when the densities are lower than the critical density of the nebular line and thus $\varepsilon_{nH}/\varepsilon_{nL} \approx 1$. Therefore, $\mu^2\omega$ is given by

$$\mu^2\omega = \frac{F(T_{[\text{O III}]_{\text{fn}}})/F(T_{\text{Bal}}) - 1}{0.04 - F(T_{[\text{O III}]_{\text{fn}}})/F(T_{\text{Bal}})}. \quad (18)$$

In Fig. 6, the lines showing the variation of $T_e([\text{O III}]_{\text{fn}})$ as a function of $T_e(\text{Bal})$ for $\mu^2\omega = 0.0, 0.1, 0.5, 1.0$ and 2.0 are plotted. We obtain an average value of $\langle \mu^2\omega \rangle = 1.0$. However, it should be borne in mind that the $\mu^2\omega$ derived by eq. (18) is a upper limit since temperature variations are actually present and contribute partly to the measured temperature discrepancies.

$\mu^2\omega$ can also be estimated by comparing $T_e([\text{O III}]_{\text{na}})$ with $T_e([\text{O III}]_{\text{fn}})$, as shown in Fig. 7. Assuming that $T_e([\text{O III}]_{\text{na}})$ is constant across the entire nebula, $\mu^2\omega$ is likewise given by

$$\mu^2\omega = \frac{F(T_{[\text{O III}]_{\text{fn}}})/F(T_{[\text{O III}]_{\text{na}}}) - 1}{0.04 - F(T_{[\text{O III}]_{\text{fn}}})/F(T_{[\text{O III}]_{\text{na}}})}. \quad (19)$$

In Fig. 7, the lines showing the variation of $T_e([\text{O III}]_{\text{fn}})$ as a function of $T_e(\text{Bal})$ for $\mu^2\omega = 0.0, 0.1, 0.5, 1.0$ and 2.0 are also plotted. An average value of $\langle \mu^2\omega \rangle = 0.4$ is obtained. It is noteworthy that the presence of temperature variations will increase $T_e([\text{O III}]_{\text{na}})$ with respect to $T_e([\text{O III}]_{\text{fn}})$, in contrast to density variations. Therefore, $\mu^2\omega$ derived from eq. (19) is a lower limit.

The upper- and lower-limit of $\mu^2\omega$ are listed in Table. 3. For a few PNe having a lower limit $(\mu^2\omega)_L = 0.0$, the effect of temperature variations on the temperature determination is larger than that of density variations, causing higher $T_e([\text{O III}]_{\text{na}})$ compared to $T_e([\text{O III}]_{\text{fn}})$. For all the PNe, the mean value of $\mu^2\omega$ is in the range from 0.4 to 1.0. Thus, we suggest that $\mu^2\omega = 0.7$ may be a representative value that can be used for a typical nebula. Adopting the density contrast $\mu \sim 100$, a representative value of the condensations filling factor ω is about 7×10^{-5} . The value is similar to that found by Viegas & Clegg (1994). Adopting $\mu^2\omega = 0.7$ for all the PNe, we obtain new $T_e([\text{O III}]_{\text{fn}})$, for which the contribution of the clumps has been deduced using equation (17). Comparing the new $T_e([\text{O III}]_{\text{fn}})$ and $T_e(\text{Bal})$, we re-evaluate the average value $\langle t^2 \rangle = 0.032$, which is in good agreement with the value yielded by the comparison of $T_e([\text{O III}]_{\text{na}})$ and $T_e(\text{Bal})$ (see Section 4.2).

4.4. The difference between temperatures derived from the [O III] forbidden lines and from the Balmer jump versus electron density

In Fig. 8, the differences between temperatures derived from the [O III] forbidden lines and from the Balmer jump are plotted against electron densities derived from the hydrogen recombination spectrum, the [O II] $\lambda 3729/\lambda 3726$, [S II] $\lambda 6716/\lambda 6731$, [Cl III] $\lambda 5517/\lambda 5537$ [Ar IV] $\lambda 4711/\lambda 4740$ and the [O III] $52\mu\text{m}/88\mu\text{m}$ ratios, respectively. In all cases, the differences between the two temperature are anti-correlated with nebular densities derived from various density indicators. A least-squares fit yields the following relation:

$$\Delta T = (1.30 \pm 0.12) \times 10^4 - (2.93 \pm 0.27) \times 10^3 \log N_e, \quad (20)$$

and a linear correlation coefficient of 0.51, where $\Delta T = T_e([\text{O III}]) - T_e(\text{Bal})$ and N_e is that derived from hydrogen recombination spectrum, which represents the average density of the entire nebula. Garnett & Dinerstein (2001) found that the discrepancies of O^{2+}/H^+ abundance ratios derived from ORLs and from CELs are greater for larger, lower-surface brightness PNe than for compact, dense ones. On the other hand, Liu et al. (2001b) found that the abundance discrepancies are greater for those with larger temperature discrepancies. Our results are therefore consistent with these earlier findings. Liu et al. (2001b) found that,

$$\Delta(\text{O}^{2+}/\text{H}^+) = (0.209 \pm 0.085) + (2.01 \pm 0.33) \times 10^{-4} \Delta T, \quad (21)$$

where $\Delta(\text{O}^{2+}/\text{H}^+) = \log(\text{O}^{2+}/\text{H}^+)_{\text{ORL}} - \log(\text{O}^{2+}/\text{H}^+)_{\text{CEL}}$. From the two relations given in equations (20) and (21), we find that the ratio of abundances derived from ORLs and from CELs has a power-law dependence on density,

$$\frac{\text{O}_{\text{ORL}}^{2+}}{\text{O}_{\text{CEL}}^{2+}} \propto N_e^{-\alpha}, \quad (22)$$

where $\alpha = 0.59 \pm 0.15$.

In general, electron densities of PNe are expected to decline monotonically as nebulae expand. Schmidt-Voigt & Koppen (1987) found an approximate relation between nebular mean electron density and nebular size, $N_e \propto R^{-3}$, where R is the nebular radius. Consequently, it is suggested that the temperature discrepancy is related to the evolutionary state of PNe; more expanded PNe show larger temperature discrepancies. On the other hand, the actual evolution in a given nebula may depend on many factors. Furthermore, the electron density measured for a given nebula may depend on the diagnostic used. For example, electron densities of low-ionization regions, as probed by the [O II] $\lambda 3729/\lambda 3726$ and [S II] $\lambda 6716/\lambda 6731$ line ratios, can be enhanced by interactions of fast stellar winds with earlier slow winds. Therefore, there are slight difference in deriving the relation of ΔT and N_e from

different density diagnostics, as shown in Fig. 8. We also use electron density derived from these forbidden line ratios to estimate the α -value in equation (22). The results show that the value is within the range of 0.3 and 0.9.

To explain the relation shown in equation (20) and (22), we apply a chemically inhomogeneous two-component model presented by Liu et al. (2000). In their hypothesis, the nebula consists of two components, H-deficient clumps and diffuse material with ‘normal’ abundances (\sim solar). These H-deficient clumps are expected to have a low electron temperature due to enhanced cooling caused by high metallicity and pressure equilibrium between the two components, so that only recombination lines are emitted. As a result, ORLs yield overestimated heavy element abundances. In a given PN, the contribution of the two components to the Balmer temperature and abundance determinations depends on their densities, i.e., the contribution becomes weaker as density declines. If the clumps have neutral cores, as found in Abell 30 (Ercolano et al. 2003) and NGC 7293 (Dyson et al. 1989), they are expected to be quite stable during the evolution of the PNe. As a result, the relative contribution of the low-density and high-temperature material to the average temperature and abundance determinations decrease as nebulae expand. Consequently, the discrepancies in temperature and abundance determinations become larger as the nebulae expand.

4.5. Are He/H ratios generally overestimated?

A long-standing problem in abundance determinations for PNe has been that the heavy element abundances derived from ORLs are systematically higher than those derived from CELs. The ratio of abundances derived from the two types of emission lines is found to vary from target to target. Tsamis et al. (2003a) analysed a PN sample and found the ORL/CEL discrepancy factors for these heavy element abundances span a range from about 2 to as large as 20. For the most extreme known PNe Hf 2-2, the ORL/CEL abundance ratio reaches a record value of 84 (Liu 2003). Another problem in nebular astrophysics is that $T_e([\text{O III}]_{\text{na}})$ are systematically higher than $T_e(\text{Bal})$, as we have discussed in § 4.2. The two problems are found to be related. A positive correlation between the ratio of O^{2+}/H^+ derived from O II ORLs and from [O III] CELs and the temperature discrepancy $[\Delta T = T_e([\text{O III}]_{\text{na}}) - T_e(\text{Bal})]$ has been shown by Liu et al. (2001b).

The explanations for the dichotomy in abundance and temperature determinations have focussed on temperature and density variations and chemical inhomogeneities. However, it has been shown that the temperature and density variations alone can be ruled out by current observations (Liu 2001, 2003). At present, the most plausible explanation is that there exist some cold H-deficient clumps in nebula (Liu et al. 2000) where only recombination lines are

emitted.

To fit the observed pattern of NGC 6153, Liu et al. (2000) have presented several empirical models incorporating H-deficient clumps. Péquignot et al. (2003) also constructed photoionization models of NGC 6153 and M 1-42, incorporating H-deficient clumps, which reproduce the observed integrated line ratio satisfactorily. In all the models, the H-deficient clumps contain only about 1% of the total mass, suggesting that the H-deficient components contain only a tiny amount of nebular gas. Nevertheless, they can seriously enhance the intensities of ORLs, causing overestimated ORL abundances. Therefore, the He/H abundance ratio could be overestimated owing to the existence of the H-deficient clumps can lead to since all the observable strong He I and He II lines are recombination lines. Some H-deficient components have been found in some PNe, such as Abell 30 and Abell 78 (Jacoby & Ford 1983). Wesson et al. (2003) analysed optical spectra of the H-deficient knots in Abell 30 and found the He/H abundance ratios of the knots are more than ten.

These PNe with extremely large abundance and temperature discrepancies, such as NGC 6153, M 1-42 and Hf 2-2, have been found to have high He/H abundances. Peimbert & Torres-Peimbert (1983) defined the PNe having high He/H abundance (≥ 0.125) as Type-I PNe. According to our suggestion, these PNe with high He/H abundances might result from contamination from H-deficient clumps. Quantitative analysis of overestimated He/H abundances in PNe is quite difficult. For this purpose, as mentioned by Péquignot et al. (2003), one has to rely on the measurement of He I $\lambda 10830$ line which is strongly enhanced by collisional excitation from the $2s^3S$ metastable level.

If the He/H abundance is enhanced by H-deficient clumps, one expects that there is a positive correlation between the He/H abundance and the ORL/CEL abundance ratio of heavy element. For most PNe, however, heavy element ORLs are quite weak and thus yield large uncertainties in the resultant abundance. Instead, we can study the relation between the He/H abundance and ΔT since the ORL/CEL abundance ratio has been found to be positively correlated with ΔT by Liu et al. (2001b). Fig. 9 plots He/H versus ΔT . The measurement error of the He/H abundance ratio is negligible. In the figure, filled and open circles represent the Galactic disc and bulge PNe respectively and the solid line is a linear fit represented by the relation:

$$\text{He/H} = (0.056 \pm 0.003) + (4.25 \pm 0.11) \times 10^{-5} \Delta T, \quad (23)$$

which yields a linear correlation coefficient of 0.50. Although there is considerable scatter, there is a trend of increasing He/H abundance with increasing difference between the temperature from [O III] forbidden lines and Balmer discontinuity for both the Galactic disc and bulge PNe. Therefore, it seems plausible that the He/H abundances in PNe have been generally overestimated due to the existence of cold H-deficient clumps.

Fig. 9 also shows that the most of PNe have enhancement of helium with respect to the Sun, which is often ascribed to the second and third dredge-up. However, the normal model of dredge-up cannot explain some extreme cases, such as He 2-111 which has a He/H abundance of 0.219 (Kingsburgh & Barlow 1994). For these cases, the more likely reason is that pollution of the H-deficient clumps causes an overestimate of the He/H abundance ratio. On the other hand, we cannot completely reject the possibility that helium in nebulae has been partly enhanced by the products of nucleosynthesis of the central star. That may be the main cause of the scatter in the derived He/H abundances. The presence of hydrogen-deficient clumps may be further proof.

The ORL/CEL abundance discrepancies are also found in H II regions (Esteban et al. 2002; Tsamis et al. 2003b). And the existence of some high density clumps in H II regions has been indicated by previous studies (e.g. O’Dell et al. 2003). Therefore, the H-deficient material might also be present in H II regions, leading to overestimated ORL abundances. If this is the case, the primordial helium abundance, which is based on observations of some metal poor extragalactic H II regions, could have been overestimated.

5. Temperatures and densities derived from the hydrogen recombination spectra near the Paschen jump

The hydrogen recombination spectrum near the Paschen jump can also provides a diagnostic of electron temperature and density [hereafter, $T_e(\text{Pas})$ and $N_e(\text{Pas})$]. Unfortunately, in our sample, the spectra covering the Paschen jump are available for only four PNe, NGC 7027, NGC 6153, M 1-42 and NGC 7009. Using the same method described in Section 3, we match the theoretical with the observed spectra at 8250 Å. Given that the observed spectra near the Paschen discontinuity may include a contribution from a dust emission tail, we added a constant continuum for the match. The results are shown in Fig. 10. All the spectra are normalized to P 20 in order to decrease the uncertainty of reddening correction. Table 4 lists the derived temperatures and densities. One advantage of using the spectrum near the Paschen jump is that the resultant temperature and density are not affected by the continuum of the hot central star and two-photon emission. However, the emission from local dust may be stronger in this band. In addition, the estimation of the continuum bluewards the Paschen jump is affected by the telluric absorption (H_2O and O_2). And the Ca II absorption feature might also cause a error in fitting the continuum longward of the Paschen jump of some PNe, such as M 1-42. As a result, the temperatures and densities derived from the hydrogen recombination spectra at the Paschen jump are less reliable than those derived from those at the Balmer jump.

Table 4 shows that the $N_e(\text{Pas})$ are consistent with the $N_e(\text{Bal})$ within the errors. However, the $T_e(\text{Pas})$ are found to be 4000, 1000, 500 and 1200 K lower than the $T_e(\text{Bal})$ for NGC 7027, NGC 6153, M 1-42 and NGC 7009, respectively. This may be due to systematic errors in the reddening correction or flux calibration. As an alternative, it remains possible that the discrepancy is caused by temperature variations. Further investigations including a larger data sample of PNe is needed to clarify the point.

6. Summary

In this work, we presented a method to derive nebular electron temperature and density simultaneously by matching the theoretical with the observed hydrogen recombination spectra. Using the method, we derived electron temperatures and densities of 48 Galactic PNe. The temperatures and densities derived by this method are compared with those derived from other indicators, enabling us to study electron temperature and density variations in PNe. Our main findings are as follows.

- The densities derived from hydrogen recombination spectra are generally higher than those deduced from forbidden line ratios, suggesting that condensations are generally present in nebulae.
- The temperatures derived from the nebular-auroral line ratios of [O III] are systematically higher than those derived from hydrogen recombination spectra, suggesting that temperature variations are generally present in nebulae. We obtained the rms temperature fluctuation parameter $t^2 = 0.031$ as a representative value.
- The larger discrepancy in temperatures derived from [O III] $(52\mu\text{m} + 88\mu\text{m})/\lambda 4959$ line ratios and from hydrogen recombination spectra, however, cannot be attributed simply to the temperature variations. The presence of clumps with $N_e \sim 10^5 \text{ cm}^{-3}$ can account well for the discrepancy. A comparison between electron temperatures derived from [O III] $(52\mu\text{m} + 88\mu\text{m})/\lambda 4959$ line ratios and those derived from hydrogen recombination spectra and [O III] $\lambda 4959/\lambda 4363$ line ratios suggests that the filling factor of the condensations has a typical value of 7×10^{-5} .
- The discrepancies in temperatures derived from [O III] $\lambda 4959/\lambda 4363$ line ratios and from hydrogen recombination spectra are related to the evolution of PNe. The ORL/CEL abundance ratio is found to have a power-law dependence on electron density ($\sim N_e^\alpha$, $\alpha = 0.59 \pm 0.15$). We attribute this to different evolutionary scenario of two components in PNe, i.e. expanding diffuse nebular material and stable cold H-deficient clumps. The

contribution of the clumps to the temperature and abundance determinations increases as the nebulae expand.

- He/H abundance has a positive correlation with the temperature discrepancy, suggesting that He/H abundances might be overestimated due to the existence of H-deficient clumps. If this is the case, traditional up-dredge theory should be modified. The primordial helium abundance determination will be affected if there are significant condensations in H II regions. Further investigations are needed.
- The densities derived from the spectrum near the Paschen jump are in good agreement with those derived from that near the Balmer jump. However, the former yield generally lower temperatures than the latter. The reason remain unknown.

We conclude that the existence of H-deficient clumps in PNe is the most plausible explanation for the origin of temperature and density variations and the ORL/CEL abundance discrepancies. However, it is a challenge to clarify the origin and evolution of these clumps. In further work, we will study the statistical relationships between the temperature and abundance discrepancies and other physical conditions of PNe such as radio flux, morphology, chemical abundances and the nature of the central star.

The authors are grateful to W. Wang for his help with part of the data reduction. We also thank J.-S. Chen and S.-G. Luo for their help with the preparation of this paper. Constructive suggestions and comments by the referee S. M. Viegas were appreciated. This work was supported in part by Beijing Astrophysics Center (BAC).

REFERENCES

- Benjamin, R. A., Skiliman, E. D., & Smits, D. P. 1999, *ApJ*, 514, 307
- Brocklehurst, M. 1972, *MNRAS*, 157, 211
- Brown, R. L., & Mathews, W. G. 1970, *ApJ*, 160, 939
- Cahn, J. H., Kaler, J. B., & Stanghellini, L. 1992, *ApJS*, 94, 399
- Dyson, J. E., Hartquist, T. W., Pettini, M., & Smith, L. J. 1989, *MNRAS*, 241, 625
- Dinerstein, H. L., Lester, D. F., & Werner, M. W. 1985, *ApJ*, 291, 561

- Ercolano, B., Barlow M. J., Storey, P. J., Liu, X.-W., Rauch, T., & Werner, K. 2003, MNRAS, 344, 1145
- Esteban, C., Peimbert, M., Torres-Peimbert, S., & Rodriguez, M. 2002, ApJ, 581, 241
- Garnett, D. R., & Dinerstein, H. L. 2001, Rev.Mex.Astron.Astrofis. Ser.de Conf., 10, 13
- Howarth, I. D. 1983, MNRAS,203, 301
- Hummer, D. G. 1988, ApJ, 327, 477
- Hummer, D. G., & Storey, P. J. 1987, MNRAS, 224, 801
- Hyung, S., Aller, L. H., & Feibelman, W. A. 1994, ApJS, 93, 465
- Jacoby, G. H., & Ford, H. C. 1983, ApJ, 266, 298
- Kingsburgh, R. L., & Barlow, M. J. 1994, 271, 257
- Kwok, S. 2000, The Orgin and Evolution of Planetary Nebulae. Cambridge University Press
- Liu, X.-W., 2001, RMxAC, 12, 70
- Liu, X.-W., 2003, in IAU Symp. 209, Planetary Nebulae, eds. S. Kwok, M. Dopita, R. Sutherland (San Francisco: ASP), p.339
- Liu, X.-W., Storey, P. J., Barlow, M. J., Danziger, I. J., Cohen, M.,& Bryce, M. 2000, MNRAS, 312, 585
- Liu, X.-W., Barlow, M. J., Cohen, M., Danziger, I. J., Lou, S.-G., Baluteau, J. P., Cox P., Emery, R. J., Lim, T., & Pequignot, D. 2001a, MNRAS, 323, 343
- Liu, X.-W., & Danziger, I. J., 1993, MNRAS, 263, 256
- Liu, X.-W., Luo, S.-G., Barlow, M. J., Danziger, I. J., & Storey P. J. 2001b, MNRAS, 327, 141
- O'Dell, C. R., Peimbert, M., & Peimbert, A. 2003, AJ, 125, 2590
- Osterbrock, D. 1989, Astrophysics of Gaseous Nebulae and Active Galactic Nuclei. University Science Books, Mill Valley, CA
- Peimbert, M. 1967, ApJ, 150, 825
- Peimbert, M. 1971, Bol. Obs. Tonantzintla Tacubaya, 6, 29

- Peimbert M., Torres-Peimbert S., 1983, in IAU Symp. 103, Planetary Nebulae, ed. D. R. Flower (Dordrecht: D. Reidel), p.233
- Péquignot, D., Liu, X.-W., Barlow, M. J., Storey, P. J., & Morisset, C. 2003, in IAU Symp. 209, Planetary Nebulae, eds. S. Kwok, M. Dopita, R. Sutherland (San Francisco: ASP), p.347
- Rubin, R. H. 1989, ApJS, 69, 897
- Schmidt-Voigt, M., & Koppen, J. 1987, A&A, 174, 223
- Storey, P. J., & Hummer, D. G. 1991, Computer Phys. Commun. 66, 129
- Storey, P. J., & Hummer, D. G. 1995, MNRAS, 272, 41
- Torres-Peimbert, S., & Peimbert, M. 2003, in IAU Symp. 209, Planetary Nebulae, eds. S. Kwok, M. Dopita, R. Sutherland (San Francisco: ASP), p.363
- Tsamis, Y. G., Barlow, M. J., Liu, X.-W., Danziger, I. J., & Storey, P. 2003a, in IAU Symp. 209, Planetary Nebulae, eds. S. Kwok, M. Dopita, R. Sutherland (San Francisco: ASP), p.383
- Tsamis, Y. G., Barlow, M. J., Liu, X.-W., Danziger, I. J., & Storey, P. 2003b, MNRAS, 338, 678
- Viegas, S. M., & Clegg, E. S. 1994, MNRAS, 271, 993
- Wesson, R., Liu, X.-W., & Barlow, M. J. 2003, MNRAS, 340, 253
- Zhang, Y., & Liu, X.-W. 2002, MNRAS, 337, 499
- Zhang, Y., & Liu, X.-W. 2003, A&A, 404, 545

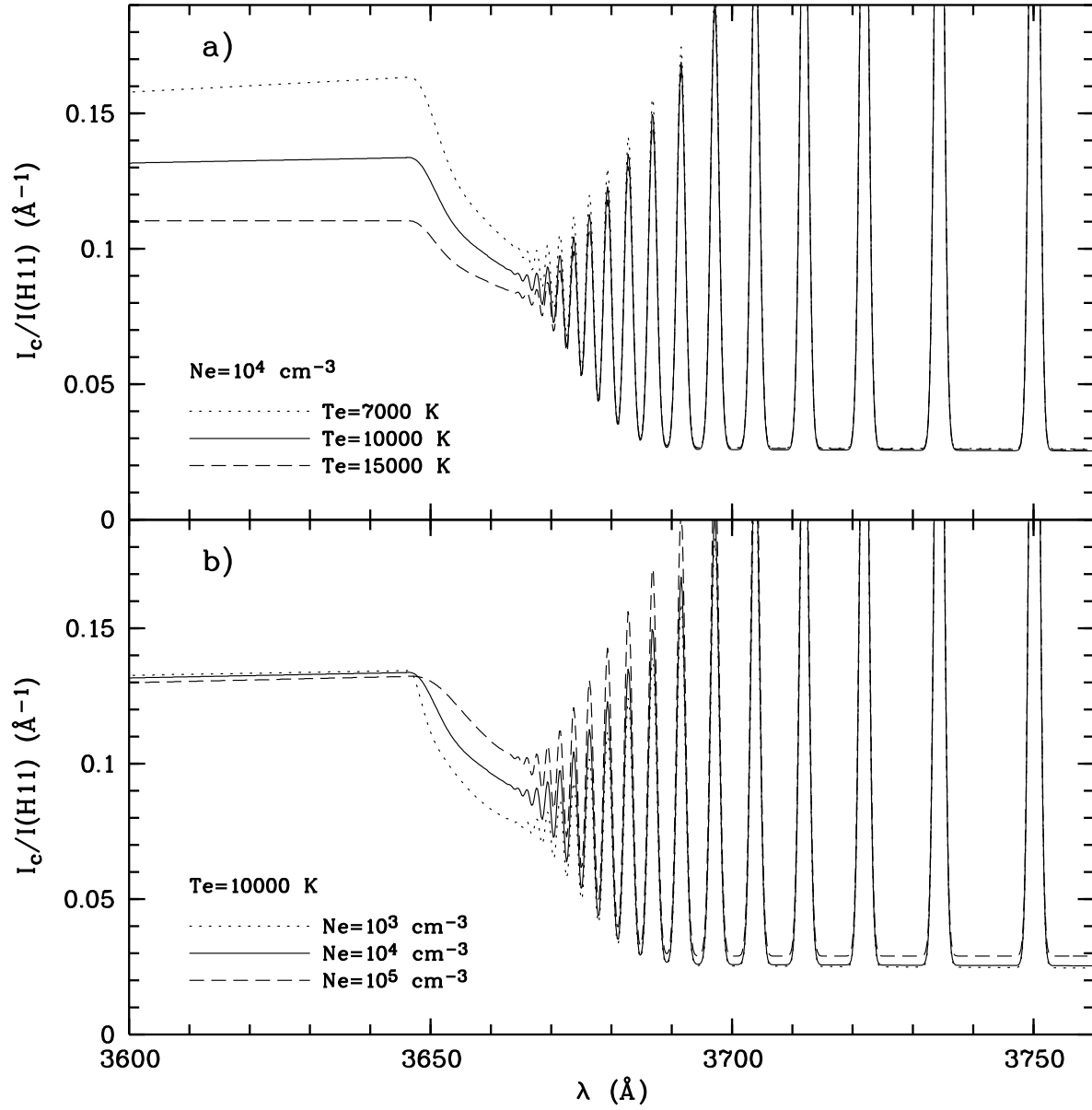


Fig. 1.— Theoretical hydrogen recombination spectra near the Balmer discontinuity at (a) same densities but different temperatures and (b) same temperatures but different densities.

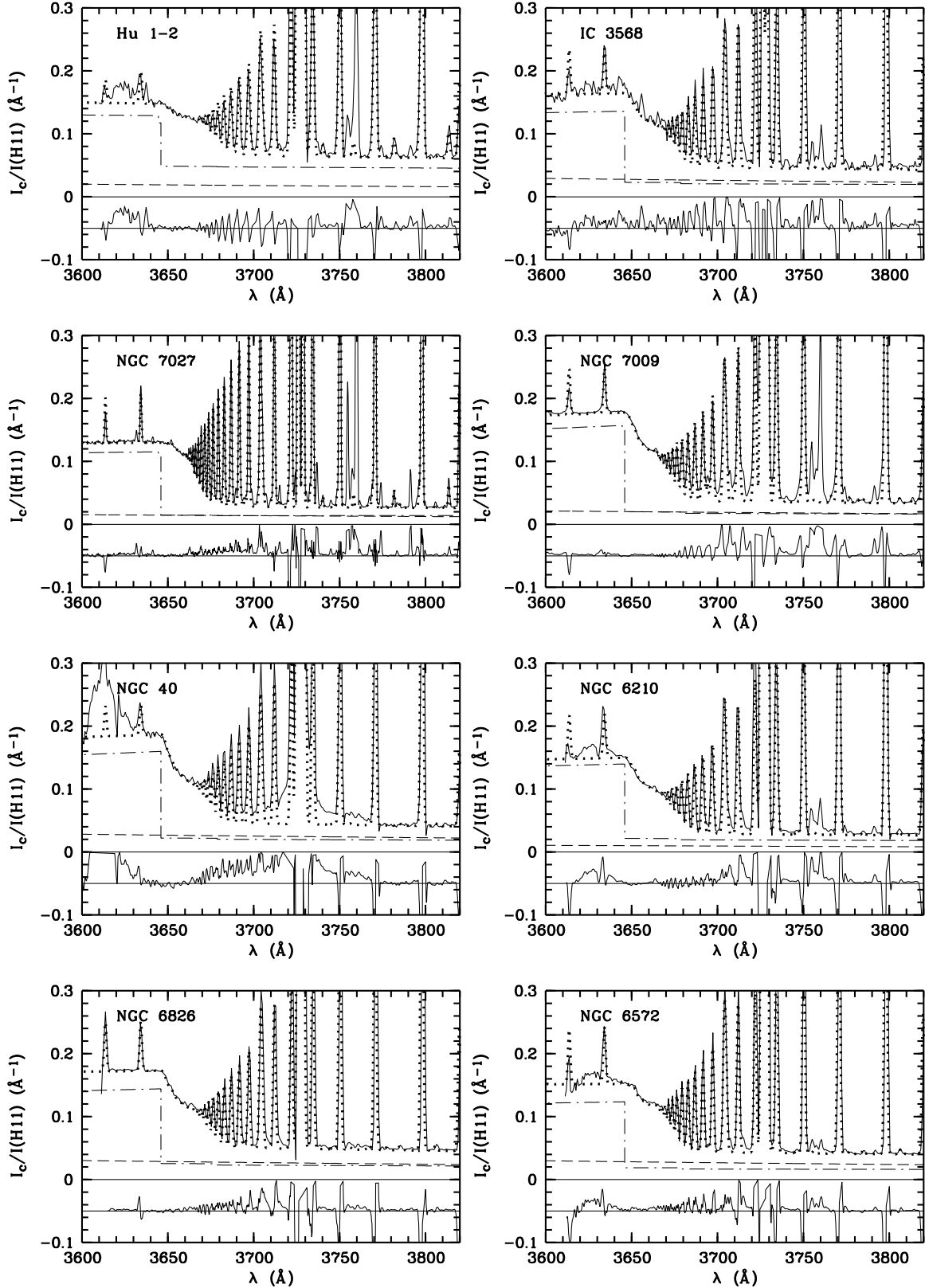


Fig. 2.— A comparison of observed and theoretical spectra at 3650 \AA . The top of each panel shows the observed spectrum (solid line) which has been de-reddened using the extinction constant listed in Table 1, the synthetic spectrum (dotted line), nebular continuum (dotted-dashed line) and stellar continuum (dashed line). The bottom shows residuals subtracted by

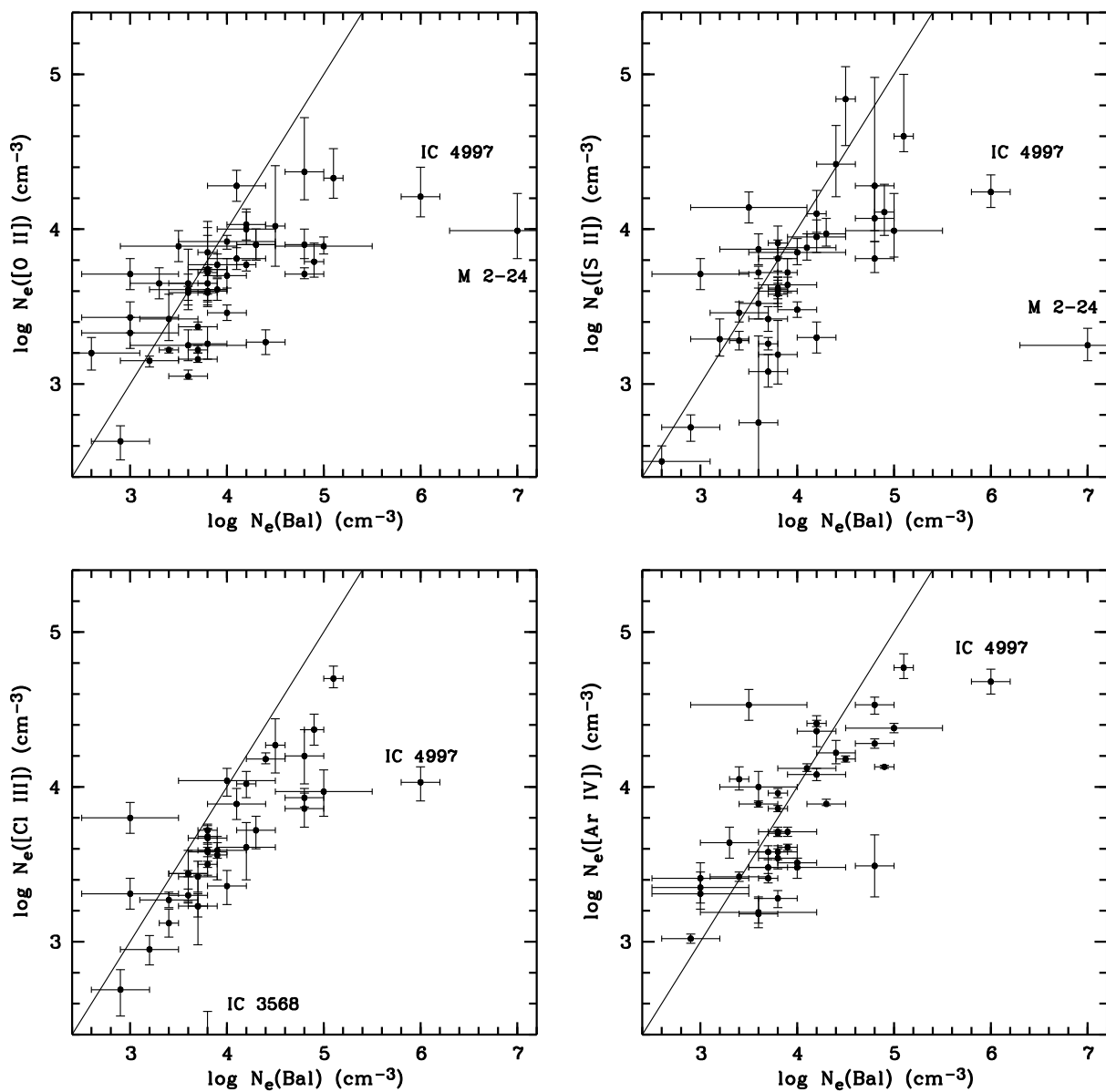


Fig. 3.— Comparison of the electron densities derived from the intensity ratios of [O II] $\lambda 3729/\lambda 3726$, [S II] $\lambda 6716/\lambda 6731$, [Cl III] $\lambda 5517/\lambda 5537$ and [Ar IV] $\lambda 4711/\lambda 4740$ versus those deduced from the Balmer decrements. The solid lines are $y = x$ plots.

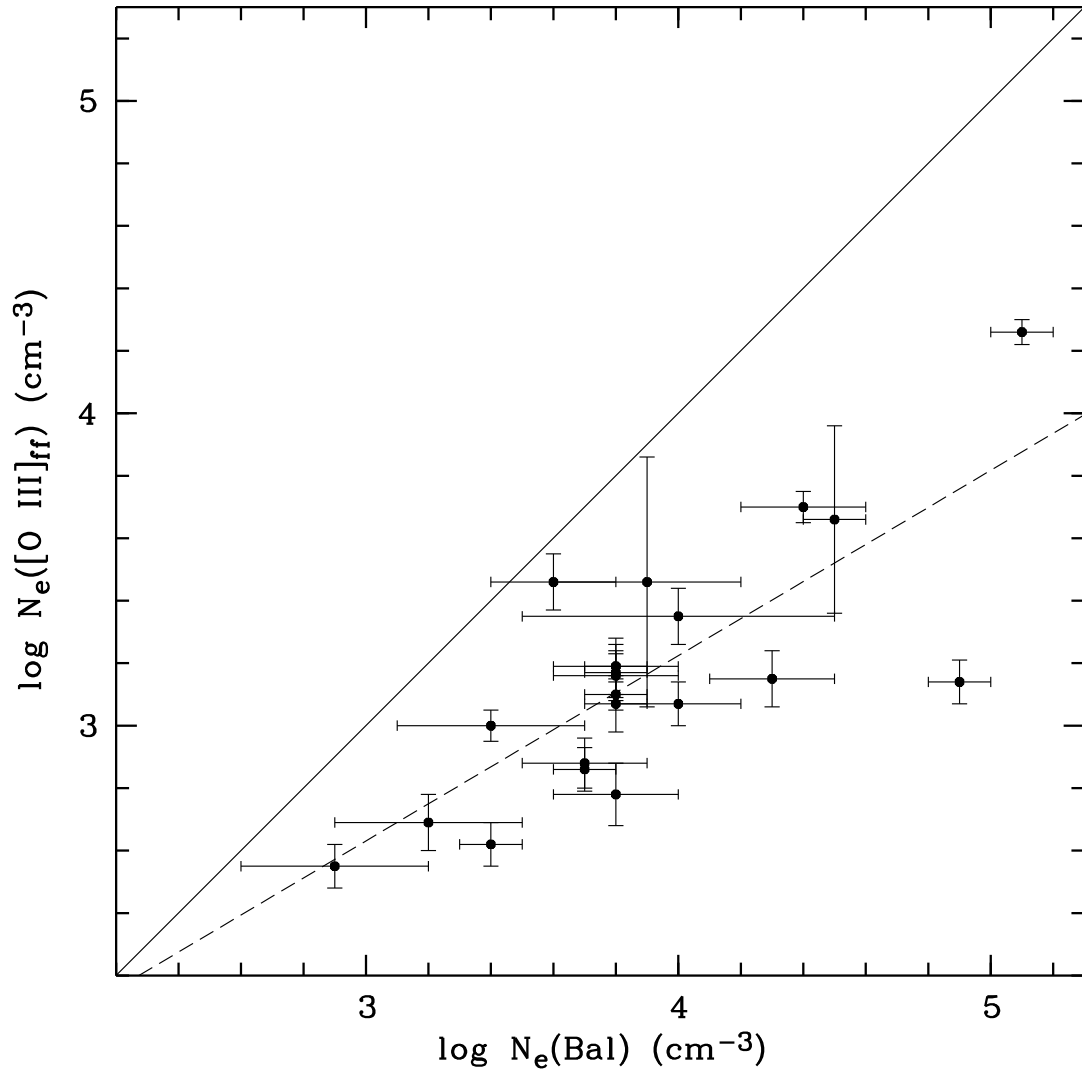


Fig. 4.— Comparison of the electron densities derived from [O III] $52\mu\text{m}/88\mu\text{m}$ ratios and the Balmer decrements. The solid line is a $y = x$ plot and the dashed line is a linear fit.

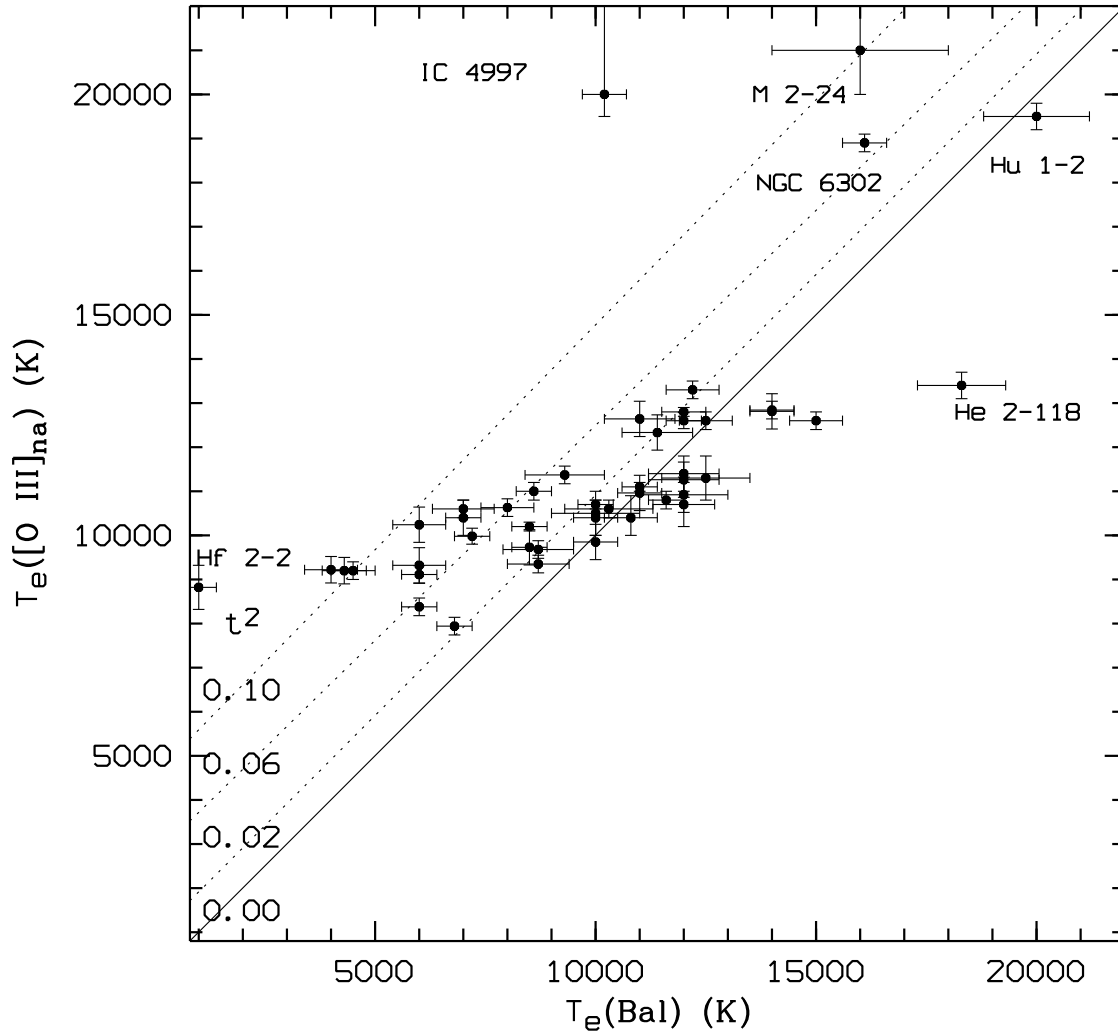


Fig. 5.— Comparison of the electron temperatures derived from the nebular-to-auroral line ratio of [O III] and those deduced from the Balmer decrements. The lines show the variation of $T_e([\text{O III}]_{\text{na}})$ as a function of $T_e(\text{Bal})$ for the mean square temperature fluctuation $t^2 = 0.00, 0.02, 0.06$ and 0.10 .

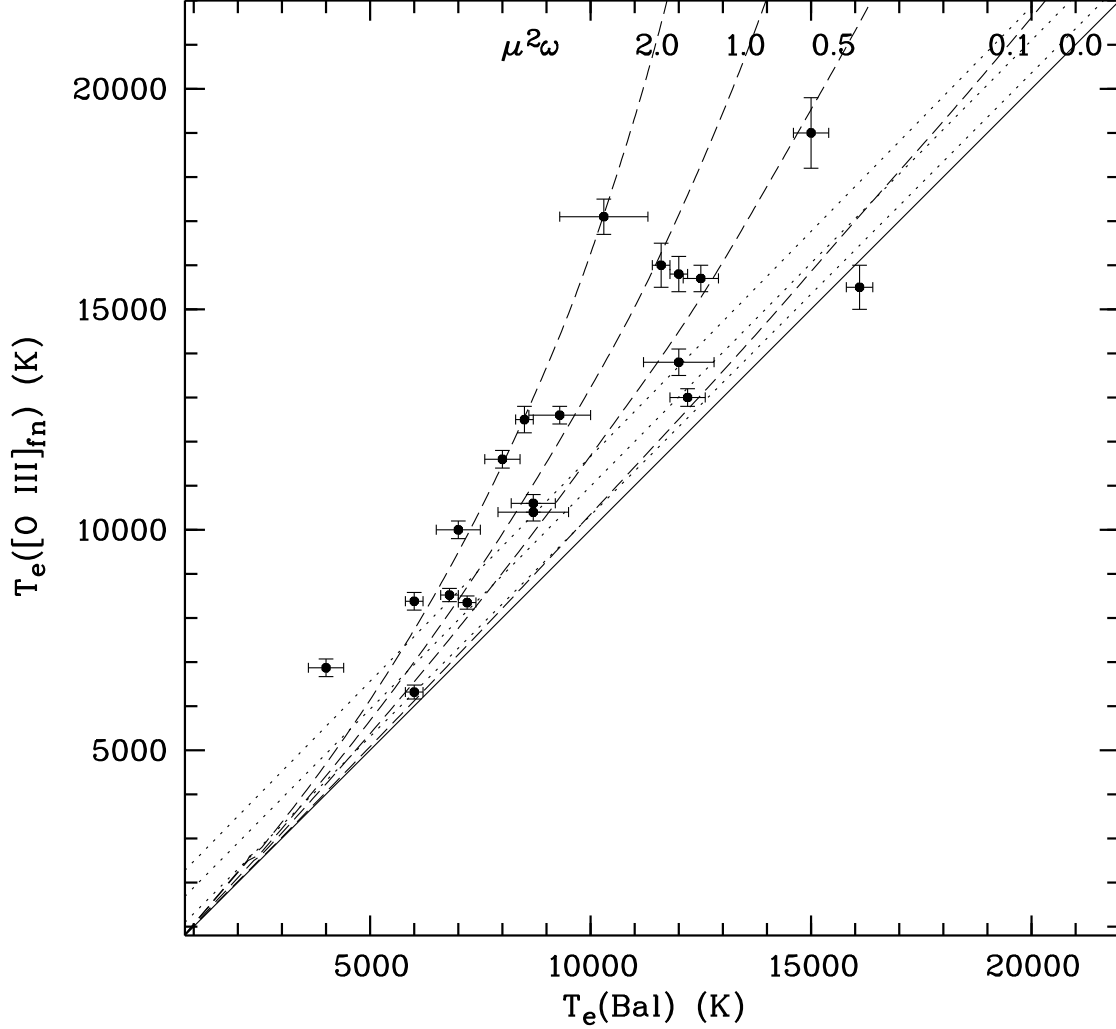


Fig. 6.— Comparison of the electron temperatures derived from the $[\text{O III}] (52\mu\text{m} + 88\mu\text{m})/\lambda 4959$ ratios and those deduced from the Balmer decrements. The dotted lines show variation of $T_e([\text{O III}]_{\text{fn}})$ as a function of $T_e(\text{Bal})$ for the mean square temperature fluctuation $t^2 = 0.02, 0.06$ and 0.10 . The dashed lines show variation of $T_e([\text{O III}]_{\text{fn}})$ as a function of $T_e(\text{Bal})$ for $\mu^2\omega = 0.1, 0.5, 1.0$ and 2.0 (see Section 4.2). The solid line shows that for homogeneous temperature and density.

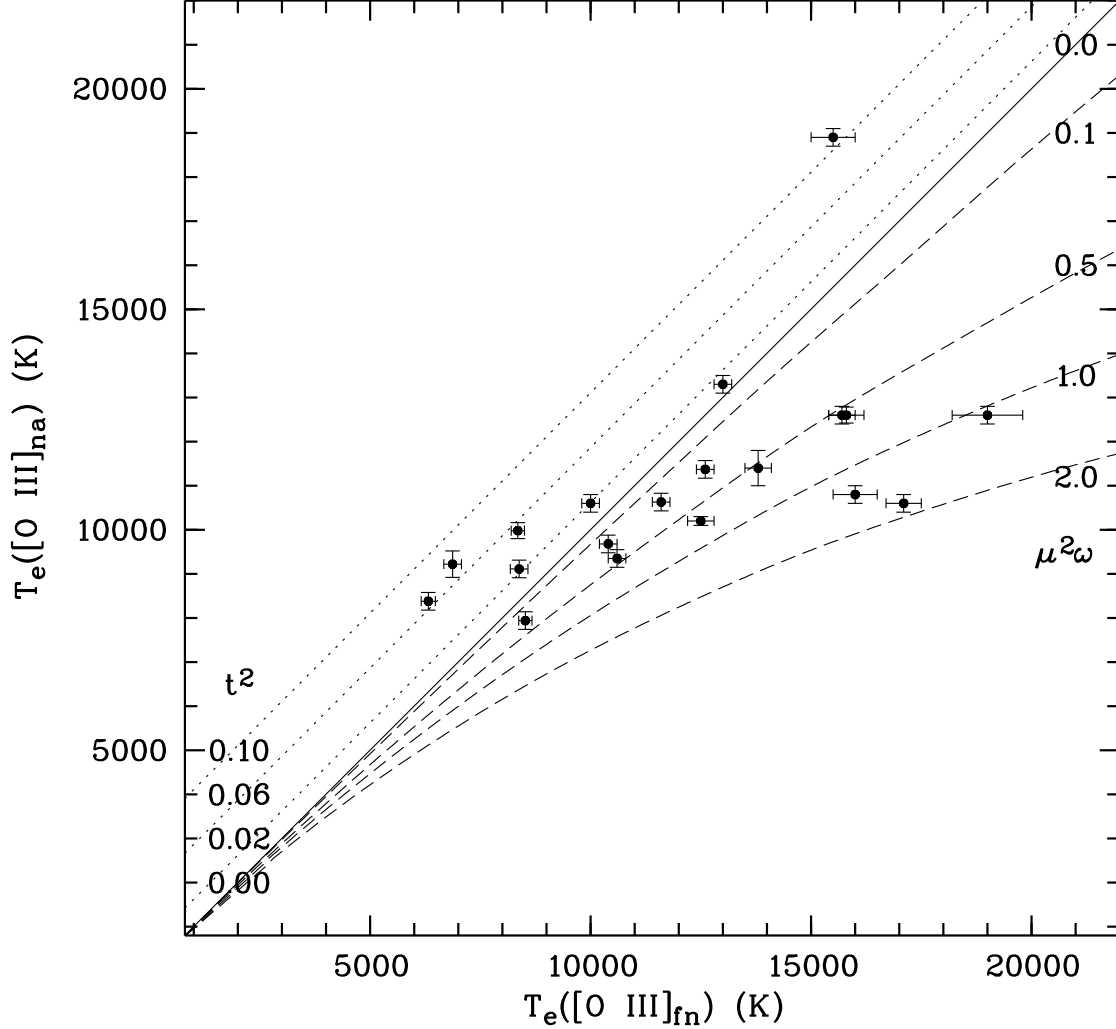


Fig. 7.— Comparison of the electron temperatures derived from the [O III] $\lambda 4959/\lambda 4363$ ratios and those deduced from the [O III] $(52\mu\text{m}+88\mu\text{m})/\lambda 4959$ ratios. The dotted lines show the variation of $T_e([\text{O III}]_{\text{na}})$ as a function of $T_e([\text{O III}]_{\text{fn}})$ for the mean square temperature fluctuation $t^2 = 0.02, 0.06$ and 0.10 . The dashed lines show the variation of $T_e([\text{O III}]_{\text{na}})$ as a function of $T_e([\text{O III}]_{\text{fn}})$ for $\mu^2\omega = 0.1, 0.5, 1.0$ and 2.0 . The solid line shows that for homogeneous temperature and density.

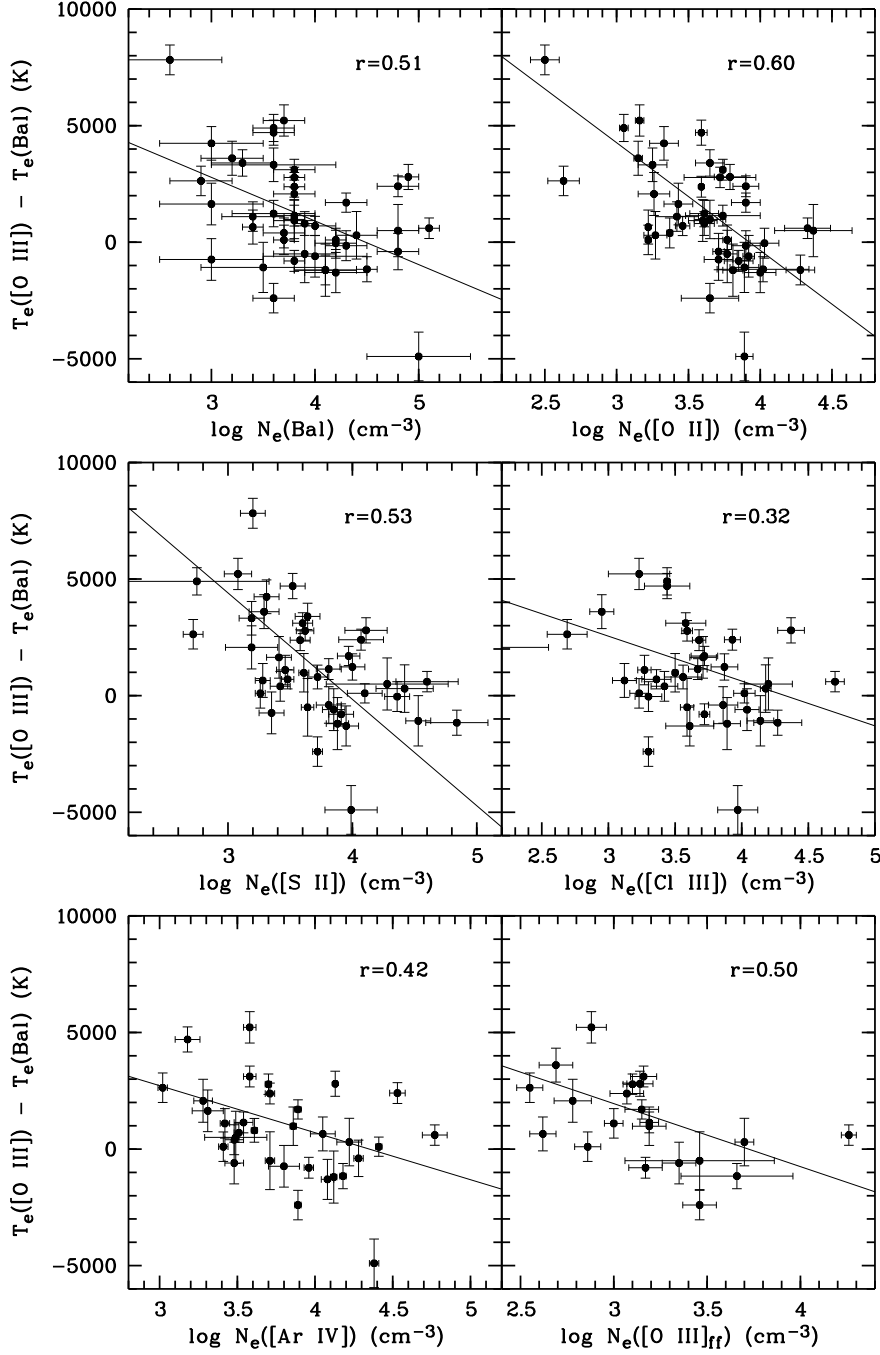


Fig. 8.— $T_e([\text{O III}]) - T_e(\text{Bal})$ versus $N_e(\text{Bal})$, $N_e([\text{O II}])$, $N_e([\text{S II}])$, $N_e([\text{Cl III}])$, $N_e([\text{Ar IV}])$ and $N_e([\text{O III}]_{\text{ff}})$. The solid lines are least-squares fits. The linear correlation coefficient “ r ” is given in every panel. For the fits the observed points are weighted according to the error bar for each. For all the cases, a trend of increasing discrepancy of temperature derived from [O III] forbidden lines and the Balmer jump with decreasing electron density is seen.

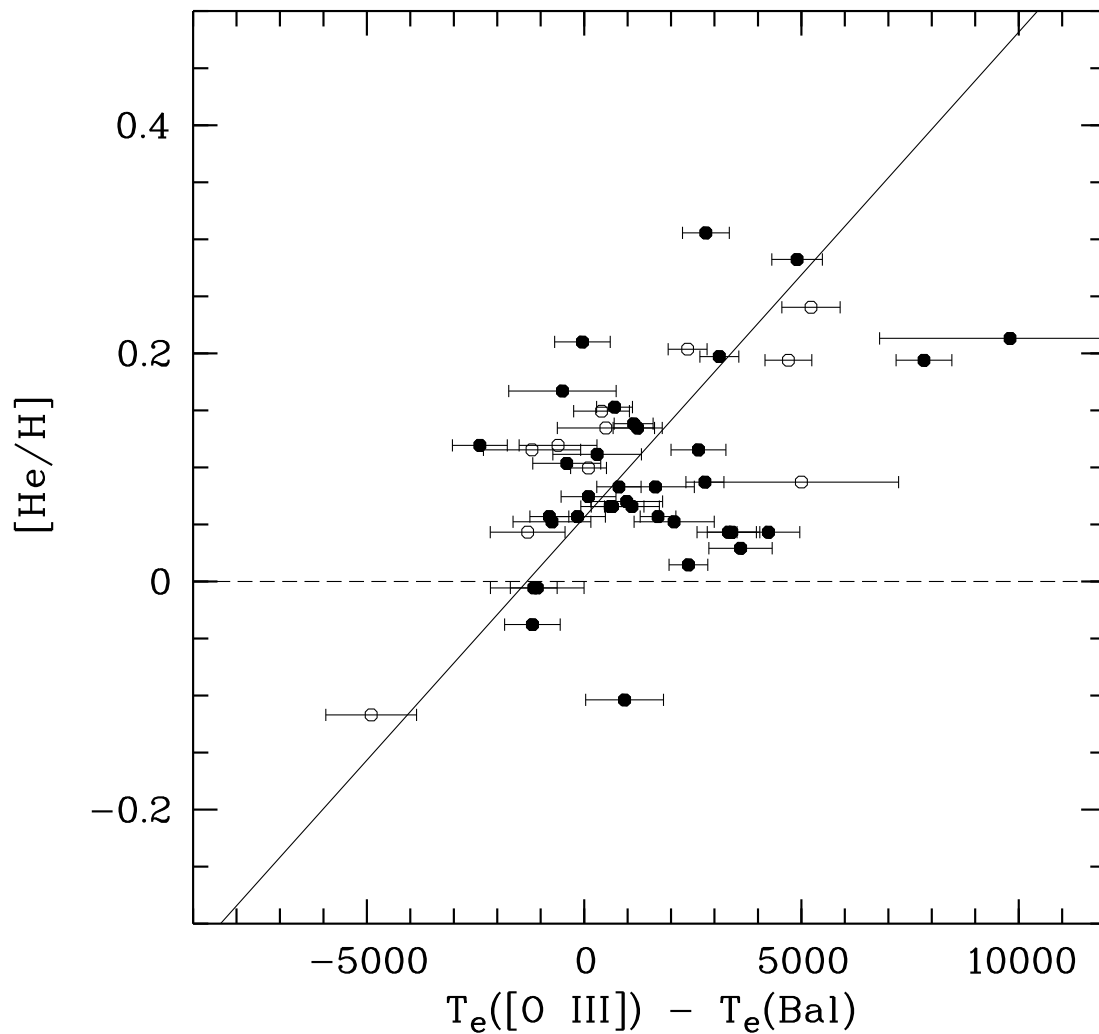


Fig. 9.— He/H versus $T_e([\text{O III}]) - T_e(\text{Bal})$. The filled and open circles are the Galactic disc and bulge PNe, respectively. The solid line is a least-squares fit. The dashed line is the solar He/H abundance. A trend of increasing He/H abundance with increasing difference between the temperature from [O III] forbidden lines and Balmer discontinuity is seen, indicating that He/H ratios in PNe may be overestimated generally.

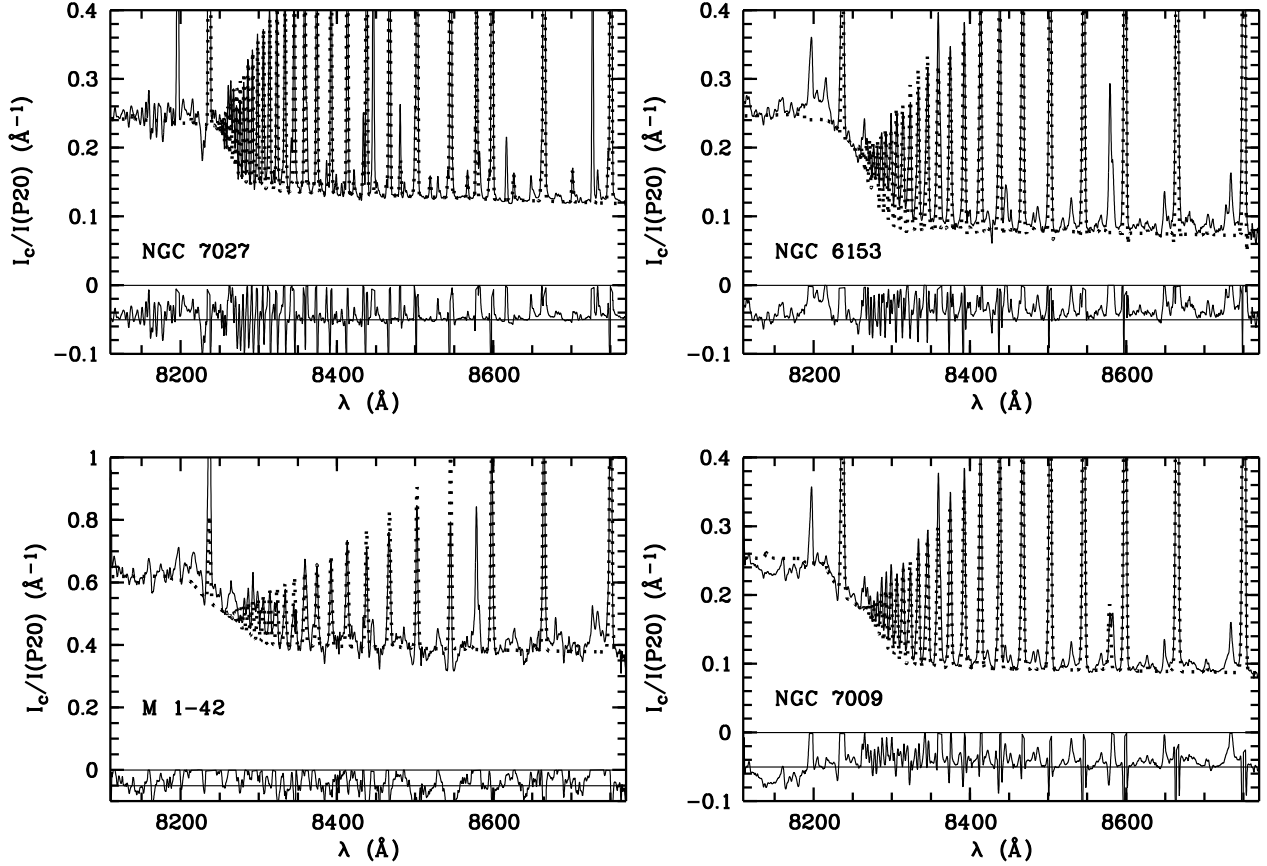


Fig. 10.— A comparison of 4 observed and theoretical spectra at 8250 \AA . The top of each panel shows the observed spectrum (solid line) which has been dereddened using the extinction constant listed in Table 1 and the synthetic spectrum (dot line). The bottom shows residuals subtracted by 0.05. Note the absorptions near 8200 \AA by atmospheric gases (H_2O and O_2) and two Ca II absorption features at 8500 \AA and 8546 \AA in the spectrum of M 1-42.

Table 1. Object and parameters; line fluxes in units of 10^{-12} erg cm $^{-2}$ s $^{-1}$.

Source	c	He $^+$ /H $^+$	He $^{2+}$ /H $^+$	T $_e$ ([O III] $_{na}$) (K)	T $_e$ ([O III] $_{fn}$) (K)	σ_o (Km/s)
Hu 1-2	0.512	0.046	0.079	19500 \pm 300	–	144
IC 3568	0.261	0.095	0.001	11370 \pm 200	12600 \pm 200	132
NGC 7027	1.380	0.058	0.041	12600 \pm 180	15800 \pm 3000	82
NGC 7009	0.130	0.093	0.011	9980 \pm 180	8350 \pm 150	132
NGC 40	0.700	0.062	0.000	10600 \pm 200	10000 \pm 200	132
NGC 6210	0.055	0.099	0.001	9680 \pm 200	10400 \pm 200	148
NGC 6826	0.064	0.099	0.000	9350 \pm 200	10600 \pm 200	132
NGC 6572	0.400	0.110	0.000	10600 \pm 200	17100 \pm 200	132
NGC 6741	1.100	0.081	0.031	12600 \pm 200	19000 \pm 2000	132
NGC 6790	1.100	0.081	0.003	12840 \pm 200	–	132
NGC 6884	1.050	0.081	0.016	10800 \pm 200	21000 \pm 1000	132
NGC 7662	0.180	0.061	0.038	13300 \pm 200	13000 \pm 200	156
NGC 6543	0.100	0.117	0.000	7940 \pm 200	8520 \pm 150	140
M 2-24	0.800	0.099	0.005	21000 \pm 1500	–	156
Cn 2-1	1.063	0.104	0.004	10400 \pm 500	–	132
NGC 6720	0.200	0.094	0.017	10630 \pm 200	11600 \pm 200	132
NGC 6620	0.760	0.099	0.021	10400 \pm 400	–	132
NGC 6567	0.670	0.105	0.007	11400 \pm 400	13800 \pm 300	132
H 1-35	1.360	0.115	0.001	10500 \pm 500	–	132
H 1-50	0.700	0.100	0.011	11300 \pm 500	–	132
He 2-118	0.158	0.065	0.000	13400 \pm 300	–	148
M 1-20	1.200	0.094	0.000	10700 \pm 500	–	123
M 3-21	0.570	0.100	0.007	11100 \pm 100	–	140
M 3-32	0.579	0.120	0.013	9200 \pm 200	–	140
IC 1297	0.220	0.079	0.042	10700 \pm 100	–	132
IC 4634	0.454	0.097	0.000	10200 \pm 100	12500 \pm 300	140
IC 4776	0.265	0.088	0.000	11000 \pm 200	–	136
IC 4997	0.438	0.139	0.000	20000 \pm 1500	–	127
NGC 5873	0.004	0.063	0.040	12800 \pm 100	–	127

Table 1—Continued

Source	c	He ⁺ /H ⁺	He ²⁺ /H ⁺	T _e ([O III] _{na}) (K)	T _e ([O III] _{fm}) (K)	σ_o (Km/s)
NGC 5882	0.380	0.113	0.003	–	–	127
NGC 6302	1.460	0.105	0.067	18900 ± 200	15500 ± 500	132
NGC 6818	0.400	0.050	0.051	12600 ± 200	15700 ± 300	148
NGC 6153	1.300	0.123	0.011	9110 ± 200	8380 ± 200	148
M 2-36	0.270	0.133	0.003	8380 ± 200	8380 ± 160	148
M 1-42	0.700	0.139	0.009	9220 ± 300	6870 ± 200	140
NGC 6778	0.890	0.155	0.008	9200 ± 300	–	140
Hf 2-2	0.200	0.131	0.002	8820 ± 500	–	132
DdDm 1	0.137	0.060	0.000	12330 ± 700	–	99
Hu 2-1	0.777	0.097	0.000	9850 ± 300	–	99
IC 2003	0.347	0.054	0.049	12640 ± 400	–	99
IC 5217	0.501	0.088	0.008	11260 ± 400	–	115
Me 2-2	0.343	0.138	0.000	10960 ± 300	–	90
NGC 6803	0.869	0.112	0.004	9730 ± 300	–	107
NGC 6807	0.642	0.084	0.000	10920 ± 500	–	107
NGC 6833	0.000	0.078	0.000	12810 ± 400	–	99
NGC 6879	0.401	0.091	0.003	10400 ± 600	–	99
NGC 6891	0.287	0.094	0.000	9320 ± 300	–	115
Vy 1-1	0.421	0.094	0.000	10240 ± 600	–	99

Table 2. Electron temperatures and densities derived from the spectra near the Balmer jump and forbidden line ratios.

Source	$T_e(\text{Bal})$ (K)	$\log N_e(\text{Bal})$ (cm^{-3})
Hu 1-2	20000 ± 1200	3.9 ± 0.3
IC 3568	9300 ± 900	3.8 ± 0.2
NGC 7027	12000 ± 400	5.1 ± 0.1
NGC 7009	7200 ± 400	3.8 ± 0.1
NGC 40	7000 ± 700	3.2 ± 0.3
NGC 6210	8700 ± 800	3.8 ± 0.1
NGC 6826	8700 ± 700	3.4 ± 0.1
NGC 6572	10300 ± 1000	4.4 ± 0.2
NGC 6741	15000 ± 600	3.6 ± 0.2
NGC 6790	14000 ± 500	4.5 ± 0.1
NGC 6884	11600 ± 400	3.8 ± 0.1
NGC 7662	12200 ± 600	3.4 ± 0.3
NGC 6543	6800 ± 400	3.8 ± 0.2
M 2-24	16000 ± 2000	7.0 ± 0.7
Cn 2-1	10800 ± 600	4.8 ± 0.2
NGC 6720	8000 ± 600	2.9 ± 0.3
NGC 6620	10000 ± 500	3.7 ± 0.2
NGC 6567	12000 ± 800	4.0 ± 0.5
H 1-35	10000 ± 1000	4.8 ± 0.2
H 1-50	12500 ± 1000	4.1 ± 0.3
He 2-118	18300 ± 1000	5.0 ± 0.5
M 1-20	12000 ± 700	4.2 ± 0.3
M 3-21	11000 ± 400	4.2 ± 0.1
M 3-32	4500 ± 500	3.6 ± 0.2
IC 1297	10000 ± 400	4.0 ± 0.2
IC 4634	8500 ± 400	4.3 ± 0.2
IC 4776	8600 ± 400	4.8 ± 0.2
IC 4997	10200 ± 500	6.0 ± 0.2
NGC 5873	12000 ± 500	3.9 ± 0.1
NGC 5882	6800 ± 500	4.0 ± 0.2

Table 2—Continued

Source	$T_e(\text{Bal})$ (K)	$\log N_e(\text{Bal})$ (cm^{-3})
NGC 6302	16100 ± 500	4.9 ± 0.1
NGC 6818	12500 ± 600	3.7 ± 0.1
NGC 6153	6000 ± 400	3.8 ± 0.2
M 2-36	6000 ± 400	3.8 ± 0.1
M 1-42	4000 ± 600	3.7 ± 0.2
NGC 6778	4300 ± 500	3.6 ± 0.2
Hf 2-2	1000 ± 400	2.6 ± 0.5
DdDm 1	11400 ± 800	3.8 ± 0.2
Hu 2-1	10000 ± 500	4.3 ± 0.2
IC 2003	11000 ± 800	3.0 ± 0.5
IC 5217	12000 ± 800	3.0 ± 0.5
Me 2-2	11000 ± 500	4.2 ± 0.2
NGC 6803	8500 ± 400	3.6 ± 0.4
NGC 6807	12000 ± 1000	3.5 ± 0.6
NGC 6833	14000 ± 500	4.1 ± 0.3
NGC 6879	7000 ± 400	3.3 ± 0.3
NGC 6891	6000 ± 600	3.6 ± 0.6
Vy 1-1	6000 ± 600	3.0 ± 0.5

Table 3. The evaluation of $\mu^2\omega$.

Source	$F(T_{\text{Bal}})$	$F(T_{[\text{O III}]_{\text{fn}}})$	$F(T_{[\text{O III}]_{\text{na}}})$	$(\mu^2\omega)_{\text{H}}$	$(\mu^2\omega)_{\text{L}}$
IC 3568	0.527	0.254	0.315	1.174	0.253
NGC 7027	0.281	0.169	0.254	0.708	0.532
NGC 7009	1.210	0.720	0.433	0.730	0.
NGC 40	1.345	0.433	0.374	2.408	0.
NGC 6210	0.641	0.392	0.469	0.681	0.208
NGC 6826	0.641	0.374	0.520	0.768	0.415
NGC 6572	0.401	0.151	0.374	1.857	1.639
NGC 7662	0.271	0.238	0.228	0.145	0.
NGC 6543	1.505	0.688	0.872	1.300	0.282
NGC 6720	0.836	0.303	0.374	1.981	0.246
IC 4634	0.688	0.258	0.411	1.867	0.634
NGC 6818	0.258	0.171	0.254	0.543	0.516
NGC 6153	2.543	0.714	0.254	2.987	0.
M 2-36	2.543	2.056	0.714	0.249	0.
M 1-42	2.543	1.422	0.543	0.850	0.
Average				1.0	0.4

Table 4. Electron temperatures and densities derived from the spectra near the Paschen jump.

Source	$T_e(\text{Pas})$ (K)	$\log N_e(\text{Pas})$ (cm^{-3})
NGC 7027	8000 ± 1000	5.4 ± 0.7
NGC 6153	5000 ± 700	3.8 ± 0.5
M 1-42	3500 ± 500	3.0 ± 0.8
NGC 7009	5800 ± 900	3.5 ± 0.7